



Constructing a carbon sphere-embedded Fe⁰ for accelerating electro-peroxone oxidation effectively: The dual catalytic role with O₃ and H₂O₂

Jinxin Xie^{a,b,c}, Yang Zheng^{a,b,c}, Qizhan Zhang^{a,b,c}, Shasha Li^{a,b,c}, Jinyu Gu^{a,b,c}, Minghua Zhou^{a,b,c,*}, Chunhua Wang^d, Yang Li^d

^a Key Laboratory of Pollution Process and Environmental Criteria, Ministry of Education, College of Environmental Science and Engineering, Nankai University, Tianjin 300350, China

^b Tianjin Key Laboratory of Environmental Technology for Complex Trans-Media Pollution, College of Environmental Science and Engineering, Nankai University, Tianjin 300350, China

^c Tianjin Advanced Water Treatment Technology International Joint Research Center, College of Environmental Science and Engineering, Nankai University, Tianjin 300350, China

^d Tianjin Wanfeng Environmental Protection Technology Co., Ltd, Tianjin 300308, China

ARTICLE INFO

Keywords:

Electro-peroxone
Fe⁰@carbon sphere
6Fe²⁺
Simultaneous catalysis of O₃ and H₂O₂
•OH

ABSTRACT

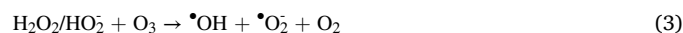
Recognizing the high energy consumption for in-situ generation of H₂O₂ and low mass transfer of O₃ in electro-peroxone (EP), Fe⁰ embedded in carbon sphere (Fe⁰@CS) was synthesized to fulfill the efficient treatment of various pollutants. At optimal condition, the degradation and mineralization of 100 mg/L phenol were 100% with *k* (0.20 min⁻¹) at 15 min and 72.1% at 60 min with iron dissolution (1.61 mg/L) and low energy consumption (0.067 kWh (g TOC)⁻¹). The utilization efficiency of O₃ and H₂O₂ increased by 1.9 – 11.5% and 16.8 – 27.1%, respectively. •Fe²⁺ originated from the faster H₂O₂ corrosion, initiated heterogeneous Fenton-like and catalytic ozonation reaction. The quenching and electron paramagnetic resonance experiments manifested the existence and mutual transformation of •OH, •O₂ and ¹O₂, among which •OH was dominant. Fe⁰@CS/EP realized the simultaneous catalysis of O₃ and H₂O₂ over wide pH 3 – 10, which had broad prospects for wastewater purification.

1. Introduction

With the development of urbanization and industrialization, the discharges of natural and synthetic organic compounds in water are increasing each year, which cause serious water pollution problems [1, 2]. In particular, the refractory organic pollutants such as phenols, chemical synthetic raw materials, antibiotics, pesticides, dyes and other toxic substances with benzene ring structures have biological genotoxicity and refractory degradability, posing great potential threat to water body and human health [3–5]. Therefore, it is urgent to take measures to remove these refractory pollutants effectively.

Peroxone technology has raised great concern because of its effectiveness and environmental friendliness for wastewater treatment, but it is limited by the transportation and storage risks of H₂O₂ [6].

Alternatively, the electro-peroxone (EP) technology can drive peroxone reaction by combining conventional ozonation and electrolysis process. It can electrochemically convert the sparged O₂ (or the mixture of O₂/O₃) into H₂O₂ (Eqs. (1) and (2)) [7], and then react with the sparged O₃ to generate •OH (Eq. (3)), which accelerates the degradation of pollutants [8,9]. Cathodic reduction of O₃ would also improve the •OH production (Eqs. (4) and (5)).



* Corresponding author at: Key Laboratory of Pollution Process and Environmental Criteria, Ministry of Education, College of Environmental Science and Engineering, Nankai University, Tianjin 300350, China.

E-mail address: zhoumh@nankai.edu.cn (M. Zhou).

<https://doi.org/10.1016/j.apcatb.2022.121935>

Received 6 July 2022; Received in revised form 26 August 2022; Accepted 1 September 2022

Available online 7 September 2022

0926-3373/© 2022 Elsevier B.V. All rights reserved.



Although the EP process improves the utilization of O_3 , there are still more than 2/3 dose of the sparged O_3 gas being discharged [10]. Specially, the limited solubility and instability of O_3 in water restricts its mass transfer efficiency [11]. With the increase of electrolysis time, the in-situ generated H_2O_2 can't be completely utilized by O_3 . What's more, the excessive H_2O_2 would consume $\bullet\text{OH}$, leading to the declination of pollutants degradation. Therefore, a large amount of O_3 waste and H_2O_2 residue exist in the EP process, enhancing the treatment cost. Consequently, it is urgent to improve the utilization of O_3 and H_2O_2 for raising efficiency and reducing the cost of EP technology for pollutant removal.

To overcome the deficiency of low utilization of O_3 and H_2O_2 , researchers have developed heterogeneous catalysts for building a gas-liquid-solid three-phase interface to prolong the contact time between the gaseous O_3 and solution because both O_3 gas and aqueous H_2O_2 pass through the catalyst interface [12]. Based on this, $\text{CuFe}_2\text{O}_4/\text{CNTs}$ were fabricated and employed for fluconazole degradation during catalytic EP reaction due to their stable crystalline structure, high magnetic response capability and catalytic activity, observing that $\text{CuFe}_2\text{O}_4/\text{CNTs}$ induced approximately 89% fluconazole transformation [13]. The presence of $\text{CuFe}_2\text{O}_4/\text{CNTs}$ could catalyze O_3 and H_2O_2 decomposition, thereby promoting $\bullet\text{OH}$ generation, which was evidenced by the lowest H_2O_2 and O_3 concentration. Moreover, in Kohantorabi's research, the naturally hematite-containing mineral of Hormuz Red Soil (C-HRS) was induced to enhance the peroxone reaction for the degradation of acetaminophen (ACT), which was ascribed to the augmented $\bullet\text{OH}$ yield through the $\text{Fe}^{3+}/\text{Fe}^{2+}$ cycle and the synergy effects between O_3 and H_2O_2 [14]. They found the residual H_2O_2 was 0.8 mM in C-HRS/ $\text{O}_3/\text{H}_2\text{O}_2$, while 9.7 mM in $\text{O}_3/\text{H}_2\text{O}_2$, demonstrating that the reaction between O_3 and H_2O_2 was further promoted by the C-HRS. Li et al. devised the high valence of Cu species generation in the framework of Si-O skeleton of MCM-48 (a mesoporous molecular sieve, CuSi-BM_{60}) by ball milling, which delivered raised H_2O_2 utilization and excellent EP catalytic performance in ROS generation ($\bullet\text{OH}$, $\bullet\text{O}_2$, $^1\text{O}_2$) for complete degradation and 73.2% mineralization of tetracycline within 60 min [15]. Mechanism showed that the complex between CuSi-BM_{60} and H_2O_2 had significantly higher chemical reactivity than pure MCM-48 clusters owing to accelerated electron transfer, which was the initiator of ozone decomposition for EP reaction. However, higher pH inhibited the target pollutants degradation because SiO-CuO^- or SiO-CuOH groups had weaker electrostatic forces on the acidic intermediates at pH 9 or pH 7. Therefore, the universality of pH need be further strengthened. In addition, although most studies have measured the concentration of O_3 and H_2O_2 in the liquid, the utilization efficiency and energy consumption have yet been calculated for evaluating the catalytic EP process. In view of the coexist of multiple reactions, it is necessary to explore the relative contribution for pollutants removal among the multiple reactions (catalytic ozonation, Fenton-like, peroxone, O_3) and clarify the possible key parameters in practical application [16]. The mechanism of simultaneous catalysis of O_3 and H_2O_2 and the corresponding reactive oxygen species are still unclear.

Zero valence iron (Fe^0) has received significant attention in AOPs due to its high reducing potential, low cost and non-toxicity [17–19]. Lai et al. setup a micro-size mFe^0/O_3 process to degrade 500 mg/L *p*-nitrophenol (*p*-NP) in aqueous solution, and 89.5% COD removal was obtained after 60 min treatment, but the released total Fe concentration was up to 231 mg/L. The reaction mechanism was consisted of homogeneous catalytic ozonation of $\text{Fe}^{2+}/\text{Fe}^{3+}$ and heterogeneous catalytic ozonation of Fe_3O_4 , Fe_2O_3 or FeOOH , as well as Fenton-like, adsorption and precipitation. Kallel et al. investigated the phenolic compounds and COD removal of olive mill wastewater by $\text{Fe}^0/\text{H}_2\text{O}_2$, founding that the treatment efficiency depended on H_2O_2 dose, pH and the organic matters concentration [20]. On account of the dual role of Fe^0 in catalyzing O_3 and H_2O_2 , a $\text{Fe}^0\text{-O}_3/\text{H}_2\text{O}_2$ process was developed for treating semi-aerobic aged refuse biofilter leachate. In the $\text{O}_3/\text{H}_2\text{O}_2$ environment, Fe^0 generated Fe^{2+} and iron oxides with homogeneous and

heterogeneous catalytic roles against $\text{O}_3/\text{H}_2\text{O}_2$ to produce ROS. Furthermore, $\text{Fe}(\text{OH})_2$ and $\text{Fe}(\text{OH})_3$ colloids contributed to the removal of organics via adsorption and precipitation [21]. Most studies focused on the direct catalysis of Fe^0 in $\text{O}_3/\text{H}_2\text{O}_2$ -based AOPs. However, traditional Fe^0 favors strong aggregation into microscale particles due to high surface energy and intrinsic magnetic interaction, resulting in high iron dissolution and iron hydroxides precipitation, as well as the characteristic of low reactivity due to the intrinsic passive layer, which brings great obstacles to the application of Fe^0 in water treatment [22,23].

Introducing supports could improve metal dispersion and prevent metal dissolution, which shed new light on design of hybrid Fe^0 for environmental remediation [24]. Porous carbon spheres (CS) have the advantageous properties of high surface area and extensive porous channels, resulting in high permeability and easy access to the interior space [25,26]. Phenolic resin (PR), a kind of metal-free cross-linked polymer, is usually obtained by poly-condensation of phenols and formaldehyde and has proved to be a good precursor for fabricating CS [27–29]. Further, Dai et al. synthesized MCS by soft-templating approach, involving the polymerization of PR in presence of cationic surfactants and subsequent carbonization at high temperature [30]. Bao et al. also took the polymerization products of phenol with formaldehyde as the precursor for the microporous-mesoporous carbon material successfully [27]. This micro-mesoporous structure could protect the metal from oxidation. Moreover, the carbon material has abundant basic sites, which is favorable for catalyzing the reaction between O_3 and H_2O_2 under acidic environment. So far, the application of the carbon material derived from PR loaded metal in EP technology of water treatment is rarely reported.

Herein, in order to realize the simultaneous catalysis with O_3 and H_2O_2 in a wide pH range, we fabricated the solid micro-mesoporous carbon spheres embedded zero valent iron ($\text{Fe}^0@\text{CS}$) to strengthen EP to treat various pollutants with low iron dissolution. The physical and chemical properties of the materials were characterized via SEM, TEM, TG-DTG, XRD, XPS, BET and Raman. And phenol was selected as the model compound because it was a typical model pollutant and did not directly receive the electrons from Fe^0 [31]. The effect of carbonization temperature, current, catalyst dosage, and initial pH on the catalytic EP process were investigated. The involved $\bullet\text{OH}$, $\bullet\text{O}_2$, $^1\text{O}_2$, H_2O_2 were analyzed by trapping experiments. The variation of ROS in different processes were also analyzed by EPR. Besides, the contribution of molecular O_3 , catalytic ozonation, Fenton-like and peroxone reactions toward phenol degradation was quantitatively evaluated. O_3 and H_2O_2 utilization efficiency were also calculated. And the protective role of carbon spheres on Fe^0 and related mechanism of $\text{Fe}^0@\text{CS}$ in catalytic O_3 and H_2O_2 were further proposed. The phenol degradation pathway and the intermediates toxicity were also analyzed in $\text{Fe}^0@\text{CS}/\text{EP}$. Finally, the reusability and environmental applicability of $\text{Fe}^0@\text{CS}$ was evaluated. This study elucidated the interactional interfacial catalysis mechanism of $\text{Fe}^0@\text{CS}$ for O_3 and H_2O_2 during the $\text{Fe}^0@\text{CS}/\text{EP}$ process.

2. Experimental sections

2.1. Preparation and characterization of catalysts

$\text{Fe}^0@\text{CS}$ was prepared by hydrothermal synthesis and hard template method. Typically, a mixture of 0.65 g Tri-block copolymer Pluronic F127 ($\text{EO}_{106}\text{PO}_{70}\text{EO}_{106}$, EO = ethyleneoxide, PO = propylene oxide, 99.0 wt%) and 0.25 g cetyltrimethylammonium bromide (CTAB) was dispersed into 50 mL distilled water and 20 mL ethanol with vigorous stirring for 15 min at 313 K. Then, 0.25 mL $\text{NH}_3\cdot\text{H}_2\text{O}$ was injected into the reaction solution. After 50 min' reaction, 0.5 g resorcinol was added. After 30 min, 0.7 mL formaldehyde solution was mixed. The mixture was stirred for 24 h at 313 K, and 5 mL 0.1 M $\text{Fe}(\text{NO}_3)_3$ was added. After stirring for 30 min, the mixture was reacted for 24 h at 100 °C in a Teflon-lined stainless-steel autoclave. The products were centrifuged, washed several times and dried overnight to obtain $\text{Fe}_x\text{O}_y@\text{PR}$, which

was calcinated in Ar atmosphere at 600 °C, 700 °C, 800 °C, 900 °C for 2 h with a heating rate of 5 °C/min to get Fe@CS-600/700/800/900, respectively. Fe@CS-800 was also marked as Fe⁰@CS.

The X-ray diffraction patterns were measured with powder X-ray diffraction (XRD, Ultima IV, Rigaku Corporation) with Cu K α radiation ($\lambda = 1.542 \text{ \AA}$, 40 kV and 30 mV) at a scanning rate 5°/min from 5° to 90°. The functional groups were detected by Fourier transform infrared (FTIR, TENSOR 37 spectrometer). X-ray photoelectron spectroscopy (XPS, ESCALAB 250Xi, Thermo Fisher Scientific) was used to analyze the elemental composition and valence. The morphology of catalyst was examined by field-emission scanning electron microscopy (FESEM, LEO-1530VP, Zeiss) and high-resolution transmission electron microscopy (HRTEM, JEM-2100f). The element composition of the catalyst was also analyzed using an Energy dispersive X-ray spectrum (EDX) and elemental mapping. The thermal stability of Fe_xO_y @PR at 30 °C – 1000 °C (5 °C/min) was measured via thermogravimetric analyses (TGA) under Ar environment. The specific surface area and pore size distribution were measured by the BET analyzer (ASAP 2460, Micromeritics). The graphitization of the catalyst was analyzed by Raman spectroscopy (Theromofisher, DXR 2xi, $\lambda_{\text{ex}} = 532 \text{ nm}$). The point of zero charge (pH_{PZC}) of the prepared catalyst was measured by a NanoSizer (Nano-ZS90, Malvern). The Tafel polarization curves were carried out to determine the corrosion potential of Fe⁰@CS. They were obtained in the potential interval of 0 – 0.7 V at a scan rate of 10 mV/s. 0.05 M Na₂SO₄ solution was served as the electrolyte, while O₃ or H₂O₂ were added successively.

2.2. Degradation experiments

A carbon black - PTFE cathode (4.0 cm × 2.0 cm), a dimensionally stable anode coated with RuO₂ (6.0 cm × 2.5 cm), and 50 mM of Na₂SO₄ were employed for the EP process. Electro-oxidation (EO), ozonation (O₃), EP, heterogeneous catalytic ozonation (Fe⁰@CS/O₃), heterogeneous electro-Fenton (Fe⁰@CS/EF) and heterogeneous EP (Fe⁰@CS/EP) treatment of 250 mL pollutant solution (100 mg/L, except for ATZ 50 mg/L) were conducted in a closed column reactor (Fig. S1, d = 5.5 cm, h = 12 cm) at room temperature. In O₃, EP, Fe⁰@CS/O₃ and Fe⁰@CS/EP, the mixed O₃/O₂ gas with 55 mg/L O₃ produced by passing a pure oxygen (99.9%) feed gas through an ozone generator (6 g/h, CFK-3A, Aikang Technology Co., China), then dispersed into the aqueous solution through a titanium aerator (diameter 25 mm, length 30 mm, porosity 35%) at a flow rate of 25 mL min⁻¹. The off-gas O₃ was minored by ozone analyzer and further adsorbed by KI solution (2 wt%). To ensure consistent environment, the pure oxygen with the same flow rate was aerated for the EO and Fe⁰@CS/EF process. Stirring was operated for better ozone dispersion in the solution. The initial pH was 5.8 without adjustment unless specified. 1 mL of liquid was withdrawn and quenched with 30 μL Na₂S₂O₃ solution at each time interval. 0.1 M H₂SO₄ and 0.1 M NaOH was used to adjust pH. The effects of applied current (25 – 100 mA), catalysts concentration (50 – 400 mg/L), pH (3.0 – 10.0) on catalytic performance in Fe⁰@CS/EP were investigated. In addition, a series of trapping agents (e.g., tert-butanol (TBA), isopropyl alcohol (IPA), furfuryl alcohol (FFA), superoxide dismutase (SOD) and catalase (CAT) were used to explore the possible active species and contribution of multiple reactions.

2.3. Analytical methods

The concentration of phenol and its oxidation products (dihydroxybenzenes and benzoquinone), *p*-nitrophenol (*p*-NP), 2,4-dichlorophenol (2,4-DCP), nitrobenzene (NB), atrazine (ATZ), 2,4-dichlorophenoxyacetic acid (2,4-D), carbamazepine (CBZ) and sulfamethazine (SMT) were analyzed by high-performance liquid chromatography (HPLC) (U3000, ThermoFisher) with a DAD detector and C18 column. Analyses of carboxylic acids were carried out on a HPLC (FL2200–2) with UV detector and Carboximix-NP column. The detection

method of different pollutants was shown in Text S2. The •OH concentration was quantified by HPLC using dimethyl sulfoxide (DMSO), 2,4-dinitrophenylhydrazine (DNPH) and phosphate buffer solution (pH = 4) [32]. The total organic carbon (TOC) of the samples was measured by TOC analyzer (Shimadzu, Japan). For the O₃-based processes, O₃ gas concentration was monitored using Ozone detectors (BMT 964, Ozone Systems Technology International Inc., Germany) connected at the inlet and outlet of the reactor to measure the in-gas and off-gas O₃ concentration. Total iron dissolution, aqueous O₃ and H₂O₂ concentration were analysed by spectrophotometry using *o*-phenanthroline method, indigo method and titanium oxalate method, respectively [16,33]. The ROS were detected by an electron paramagnetic resonance instrument (EPR, EMX nano, Bruker).

The apparent first-order rate constant was calculated by the kinetic equation Eq. (6):

$$\ln(C_0/C_t) = kt \quad (6)$$

where C_0 is the initial concentration of pollutant (mg L⁻¹), C_t is the concentration of pollutant at t min (mg L⁻¹), and t is the reaction time (min), k is the rate constant (min⁻¹).

The synergistic factor was defined as a function of the rate constant of multiple processes involved in the coupling system, which was calculated by Eq. (7) and Eq. (8), respectively [34–36]:

$$SF_{\text{Fe}^0\text{@CS/EF}} = \frac{k_{\text{Fe}^0\text{@CS/EF}}}{k_{\text{EO}} + k_{\text{Fe}^0\text{@CS/O}_2}} \quad (7)$$

$$SF_{\text{Fe}^0\text{@CS/EP}} = \frac{k_{\text{Fe}^0\text{@CS/EP}}}{k_{\text{EP}} + k_{\text{Fe}^0\text{@CS/O}_2}} \quad (8)$$

where $k_{\text{Fe}^0\text{@CS/EF}}$, k_{EO} , $k_{\text{Fe}^0\text{@CS/O}_2}$, $k_{\text{Fe}^0\text{@CS/EP}}$ are the rate constants in Fe⁰@CS/EF, EO, Fe⁰@CS/O₂ and Fe⁰@CS/EP processes, respectively. $SF_{\text{Fe}^0\text{@CS/EF}}$ and $SF_{\text{Fe}^0\text{@CS/EP}}$ are the synergistic factors of EO and Fe⁰@CS/O₂ between Fe⁰@CS/EF, EP and Fe⁰@CS/O₂ between Fe⁰@CS/EP.

The specific energy consumption (SEC, kWh g⁻¹ TOC) for TOC removal in O₃, EP, Fe⁰@CS/O₃, Fe⁰@CS/EF and Fe⁰@CS/EP process was calculated according to Eq. (9), respectively.

$$\text{SEC} = \frac{UI + rC_{\text{O}_3}}{(\text{TOC}_0 - \text{TOC}_t)V} \quad (9)$$

where V is the solution volume (L), TOC_0 and TOC_t are solution TOC at times $t = 0$ and t , respectively (mg L⁻¹), I is the current (A), and t is the reaction time (h), U is the average cell voltage (V), C_{O_3} is the in-gas O₃ concentration, r is the energy requirement for O₃ generation (10 kWh kg⁻¹ O₃) [37].

The mineralization current efficiency (MCE) was calculated by Eq. (10).

$$\text{MCE} = \frac{nFV\Delta\text{TOC}}{4.32 \times 10^7 \text{ mIt}} \times 100\% \quad (10)$$

where n is the electrons consumed per phenol molecule during its mineralization was taken as 28, F is the Faraday constant (96,487 C mol⁻¹), V is the bulk volume (0.25 L), $\Delta(\text{TOC})_{\text{exp}}$ is the TOC decay (mg L⁻¹), 4.32×10^7 is the conversion factor (3600 s h⁻¹ × 1200 mg C mol⁻¹), m represents the number of carbon atoms of phenol (6), I and t represent current (A) and time (h), respectively.

The turnover frequency (TOF) was calculated through dividing the rate constant of pollutant degradation by the catalyst concentration by Eq. (11).

$$\text{TOF} = k/C_{\text{cat}} \quad (11)$$

where k is the rate constant (min⁻¹), and C_{cat} is concentration of catalyst (g L⁻¹).

Efficiency of treatment process depends on the ozone mass transfer. O₃ mass transfer (C_{O_3}) in O₃, EP, Fe⁰@CS/O₃ and Fe⁰@CS/EP process was calculated according to Eq. (12) [38].

$$C_{O_3} = Q_g \int_0^t \{ [O_3]_{in} - [O_3]_{out} \} dt \quad (12)$$

C_{O_3} is the amount of O_3 mass transfer from gas phase to liquid phase in different processes (mg), Q_g is the gas flow rate ($L \cdot min^{-1}$), $[O_3]_{in}$ and $[O_3]_{out}$ are the in-gas and off-gas O_3 concentration (mg/L), respectively.

Typically, the mass balance of O_3 during ozonation could be expressed by Eq. (13).

$$A_t = A_c + A_o + A_a \quad (13)$$

where A_t , A_c , A_o and A_a are the amount of in-gas O_3 (mg), consumed O_3 (mg), off-gas O_3 (mg) and aqueous O_3 (mg), respectively.

The total amount of off-gas O_3 (A_o) was calculated from Eq. (14).

$$A_o = \int_0^t v [O_3]_{out} dt \quad (14)$$

where $[O_3]_{out}$, v and t are the off-gas O_3 concentration (mg/L), gas flow rate (L/min) and reaction time (min), respectively.

The accumulation of aqueous O_3 concentration was calculated from Eq. (15).

$$A_a = \int_0^t V [O_3]_{aq} dt \quad (15)$$

where V and $[O_3]_{aq}$ is the solution volume (L) and the aqueous O_3 concentration (mg/L), respectively.

Thus, the consumed O_3 amount (A_c) for pollutant degradation can be calculated by Eq. (16).

$$A_c = \int_0^t V \{ [O_3]_{in} - [O_3]_{out} \} dt - A_a \quad (16)$$

where V , $[O_3]_{in}$ and $[O_3]_{out}$ is the solution volume (L), the in-gas and off-gas O_3 concentration (mg/L), respectively.

The utilization efficiency of O_3 (OUE) can be calculated by Eq. (17) [38].

$$OUE(\%) = \frac{A_c}{\int_0^t v [O_3]_{in} dt} \times 100 \quad (17)$$

The in-gas O_3 concentration was kept at 55 mg/L with a flow rate of 25 $mL \cdot min^{-1}$.

The utilization efficiency of H_2O_2 (HUE) was calculated by Eq. (18) [39].

$$HUE(\%) = \frac{\int_0^t \{ [H_2O_2]_{blank} - [H_2O_2]_t \} dt}{\int_0^t [H_2O_2]_{blank} dt} \times 100 \quad (18)$$

where H_2O_2 blank was the generated concentration of H_2O_2 in the EO

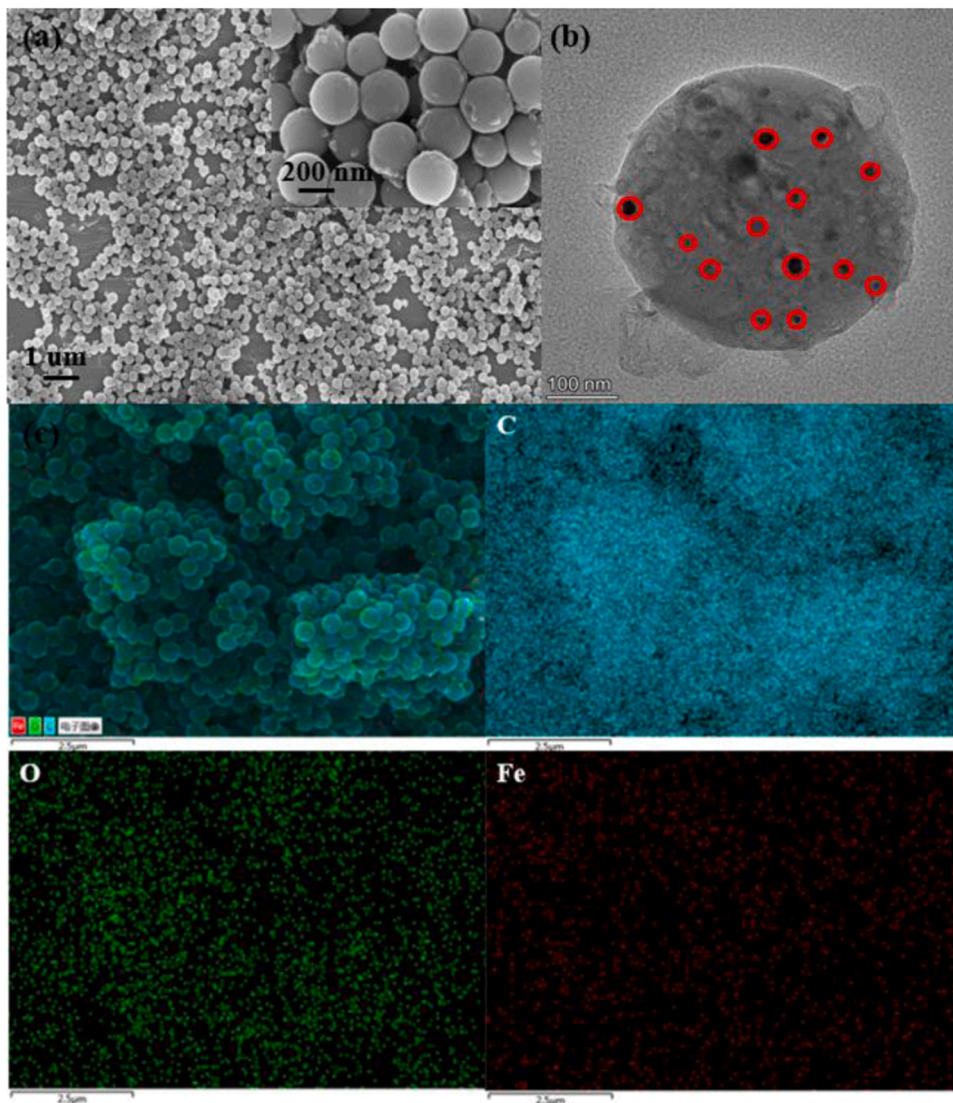


Fig. 1. (a) SEM image; (b) TEM image; (c) SEM-EDS mapping images of $Fe^0@CS$.

process, $[H_2O_2]_t$ was the H_2O_2 concentration during different processes for pollutant degradation at reaction time t ($mg\ L^{-1}$).

3. Results and discussions

3.1. Catalyst characterizations

The pure PR showed the spherical structure and uniform particle size of 400 nm (Fig. S2), which was formed with the polymerization of

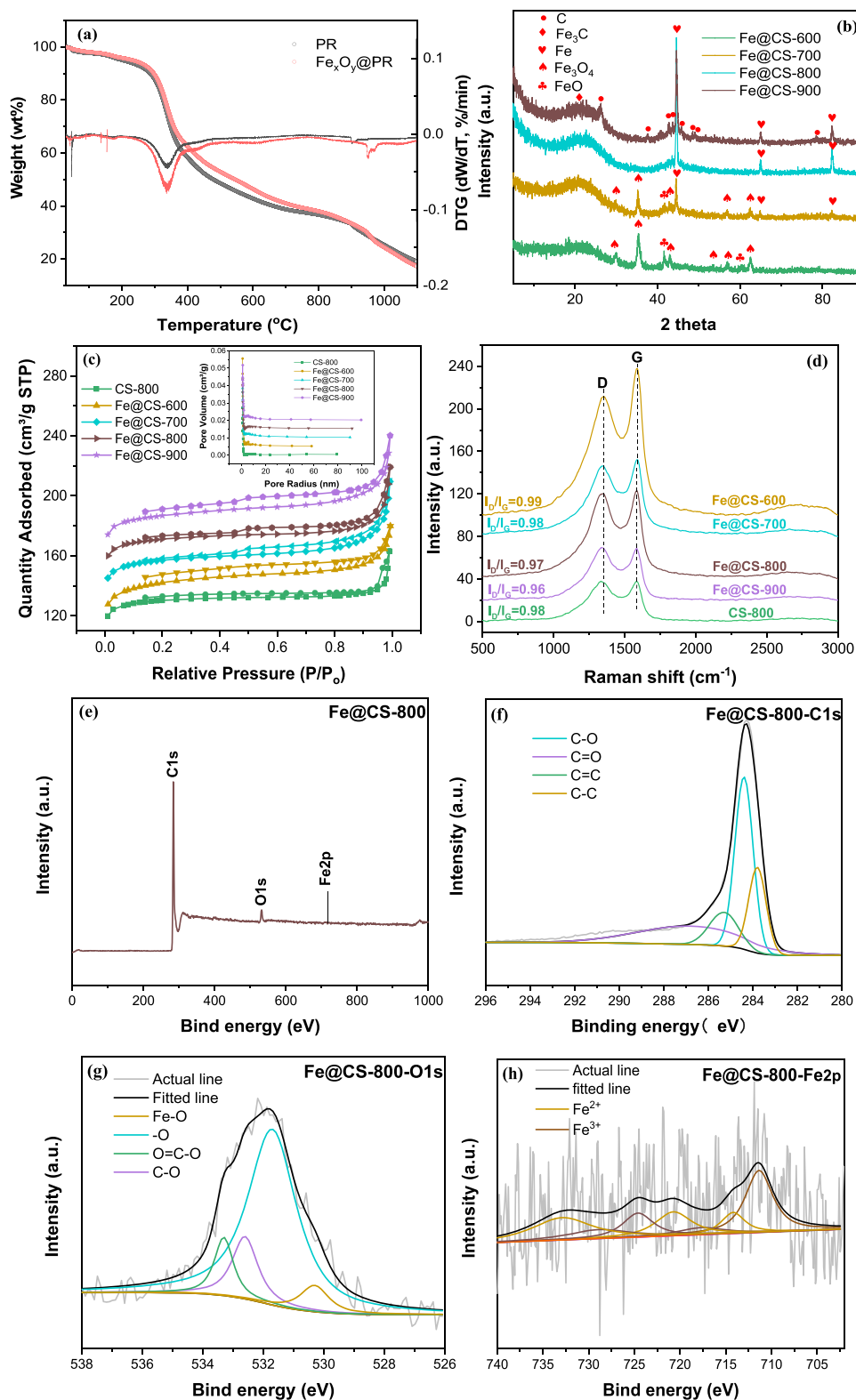


Fig. 2. (a) The TGA and DSC curve of PR and $Fe^0@PR$; (b) the XRD pattern; (c) Nitrogen adsorption and desorption isotherms at 77 K and pore size distributions; (d) Raman spectra; XPS spectra of (e) the full scan, (f) C1s, (g) O1s, (h) Fe2p.

resorcinol and formaldehyde under the function of the surfactant self-assembly. After wrapping iron particles, the structure of Fe^0/CS was the identical as the unannealed $\text{Fe}_x\text{O}_y/\text{PR}$ under the 400 nm horizon (Fig. 1a). Combined with high resolution TEM (HRTEM) images in Fig. 1b, the red circle represented the Fe^0 particles, which were embedded in the carbon sphere. Those results were in accordance with the spherical structure of Fe^0/CS . As seen in Fig. 1c, the abundance of C and O elements was high and uniformly distributed in the catalyst, while Fe element was low but well dispersed. EDX indicated the Fe content was 3.05%. (Table S1).

The TG-DTG curves (Fig. 2a) were carried out to check the thermal behavior of PR and $\text{Fe}_x\text{O}_y/\text{PR}$ in Ar atmosphere. The TG curves of PR exhibited ~40% of the residual carbon at 800 °C, indicating PR was an excellent precursor for producing carbonaceous material. The DTG curves of PR and $\text{Fe}_x\text{O}_y/\text{PR}$ had two sharp weight losses at ~280 °C and ~400 °C. The first stage of weight loss could be attributed to the physically adsorbed H_2O and violent gasification of the organic volatiles, and the second stage of weight loss might be due to the decomposition of PR resin network, which formed the carbon material of porous nature with good electrochemical properties [40,41]. As the temperature increased, the reduction of Fe_xO_y to Fe^0 resulted in further weight loss [42]. The structural evolutions of the catalysts annealed at different temperatures were investigated by using XRD, which was of more significance for catalytic E-peroxone (Fig. 2b). The wide peak at 24.5° of all samples was attributed to [002] diffraction for typical graphite carbons. At 600 °C, the diffractions at 29.9°, 35.4°, 42.9°, 53.4°, 56.8°, 62.5° of Fe_3O_4 and 41.6°, 60.5° of FeO were observed. At 700 °C, the characteristic peaks of Fe_3O_4 and FeO gradually became weaker, while the diffractions at 44.6°, 64.9° and 82.1° appeared, which were corresponded to the characteristic peaks of Fe^0 [43]. When the temperature reached 800 °C, the signals of Fe^0 became more intense and other characteristic peaks disappeared. These results suggested that Fe_3O_4 and FeO were transformed into Fe^0 with the increasing temperature. The typical diffractions of Fe_3C at 43.5° and 44.1° appeared along with the slight reduction of characteristic peak of Fe^0 at 800 °C [44].

From the N_2 adsorption-desorption isotherm and pore size distribution curve of CS-800 and $\text{Fe@CS-600/700/800/900}$ in Fig. 1c, the typical combination of type I and type IV isotherms in international Union of Pure Applied Chemistry (IUPAC) classification was observed, indicating that the samples had micropores and mesopores. A hysteresis loop at $P/P_0 = 0.1\text{--}1.0$ was observed on all samples, corresponding to the presence of mesoporous structure. The structure parameters of the catalysts were listed in Table S3. The BET surface area and pore volumes of CS-800 was 504.58 m^2/g and 0.25 cm^3/g . Comparatively, the BET surface area and pore volumes of $\text{Fe@CS-600/700/800/900}$ were 544.34, 548.79, 546.32, 546.14 m^2/g and 0.28, 0.30, 0.30, 0.29 cm^3/g , respectively. And their pores sizes were similarly centered at ~2 nm. A higher temperature led to the reduction reaction of Fe_xO_y , and carbon around iron oxide would be oxidized to CO_2 . Such reactions might act as activation processes for producing microporous and mesoporous pores in carbon spheres [45]. The influence of temperature on BET surface area and pore size distribution can be ignored.

The absorption band at 3430 cm^{-1} in the spectra of CS and Fe^0/CS were corresponded to O-H tensile vibration (Fig. S5). The adsorption bands at 2364 cm^{-1} were the C-H vibration of CH_3 and CH_2 groups of carbon materials. The adsorption band at 1531 and 983 cm^{-1} were assigned to the C=O and C-O vibration in the sp^2 -hybridized graphite carbon surface, respectively [40]. Moreover, no iron characteristic peak was observed in Fe^0/CS , which also manifested that iron species were successfully embedded in graphite carbon spheres. According to Raman spectroscopy (Fig. 2d), all samples exhibited the typical D band (1328 cm^{-1}) and G band (1582 cm^{-1}), indicating the existence of defect-site and graphitic structure. The D-band to G-band intensity ratio (I_D/I_G) was calculated to be 0.99, 0.98, 0.97 and 0.96 for $\text{Fe@CS-600/700/800/900}$, respectively. The decline of I_D/I_G value evidenced that the graphitization degree and structural stability of

samples increased, while a less content of defects existed with the increasing calcination temperature. In order to investigate the effect of metal on the graphitization degree of carbon layer, the Raman of CS-800 was also performed ($I_D/I_G = 0.98$). The lower ratio of Fe@CS-800 suggested the addition of iron promoted the graphitization of CS-800, which was advantageous to the structural stability and electron transfer ability of the catalyst [23]. Fig. 2e presented the full XPS spectra of Fe@CS-800 , where C, O and little Fe were found to exist on the surface of the sample. The spectrum of C1 s (Fig. 2f) could be deconvoluted into four peaks corresponding to C-C (283.8 eV), C-O (284.4 eV), C=C (285.3 eV), and C=O (286.8 eV), respectively. The O1s spectra (Fig. 2g) of the Fe@CS-800 was deconvoluted into four peaks, which located at 530.3, 531.7, 532.6, and 533.3 eV were ascribed to Fe-O, the absorbed oxygen (-O), C-O and -COOH, respectively. Due to the inevitable iron residue on the surface of Fe@CS-800 during the preparation process, there was quite weak signal of Fe2p, which could be fitted to seven peaks. Peaks at 714.19, 720.71, 732.9 and 711.35, 717.68, 724.6, 728.85 eV were ascribed to Fe^{2+} and Fe^{3+} , respectively.

3.2. Evaluation of catalytic activity

As shown in Fig. 3a, the degradation efficiency of phenol increased first and then decreased with the increasing calcination temperature from 600 °C to 900 °C. The phenol degradation followed the apparent first-order reaction kinetics, and the rate constant k for $\text{Fe@CS-600/700/800/900}$ were 0.10, 0.16, 0.20 and 0.20 min^{-1} , respectively (Fig. 3b). The good performance of Fe@CS-800 derived from the increasing Fe^0 sites [31]. Moreover, calcination at 600 °C and 700 °C might convert iron (III) hydroxide to be FeO and Fe_3O_4 , resulting in a lower catalytic degradation rate. When the calcination temperature reached 800 °C or above, iron oxides would be reduced by carbon to Fe^0 . Therefore, Fe@CS-800 and Fe@CS-900 showed similar activity for phenol degradation in EP. However, total Fe dissolution were 1.51, 1.56, 1.61 and 2.2 mg/L corresponding to $\text{Fe@CS-600/700/800/900}$, respectively (Fig. 3a). The increased iron dissolution possibly due to the increase of pore volume and pore diameter at higher calcination temperature. The TOC removal were 50.2%, 58.0%, 71.2% and 71.1% corresponding to $\text{Fe@CS-600/700/800/900}$ (Fig. 3b), which was consistent with the trend of degradation efficiency. Therefore, Fe@CS-800 (Fe^0/CS) was preferable for the next experiment.

3.3. Phenol removal by different processes

There are multiple catalytic reactions (including EO, ozonation, $\text{Fe}^0/\text{CS}/\text{O}_3$, $\text{Fe}^0/\text{CS}/\text{EF}$ and EP) for phenol removal by the $\text{Fe}^0/\text{CS}/\text{EP}$ process. The synergy and contribution of different reactions need to be further investigated. As shown in Figs. 4a and 4b, the phenol degradation and k value at 30 min were 66.5% and 0.042 min^{-1} in $\text{Fe}^0/\text{CS}/\text{O}_2$. This was because Fe^0 -embedded in carbon spheres could reduce oxygen to generate H_2O_2 and Fe^{2+} , resulting in Fenton-like reaction [46]. The greater phenol removal at 30 min by $\text{Fe}^0/\text{CS}/\text{EF}$ (52.3%, $k = 0.027 \text{ min}^{-1}$) and $\text{Fe}^0/\text{CS}/\text{O}_3$ (100.0%, $k = 0.115 \text{ min}^{-1}$) were higher than those of EO (6%, $k = 0.003 \text{ min}^{-1}$) and ozonation (94.7%, $k = 0.081 \text{ min}^{-1}$), which indicated Fe^0/CS could catalyze H_2O_2 and O_3 , respectively. And the phenol degradation in $\text{Fe}^0/\text{CS}/\text{O}_2$ was 65% with k 0.042 min^{-1} in 30 min. As described in Eq. (7), the SF in $\text{Fe}^0/\text{CS}/\text{EF}$ between the EO and $\text{Fe}^0/\text{CS}/\text{O}_2$ systems was found to be 0.6. This phenomenon indicated that H_2O_2 produced at CB-PTFE cathode by EO was excessive, which could captured $\cdot\text{OH}$ [47]. In EP/CS, the phenol removal at 30 min was 90.0% with k of 0.082 min^{-1} , which was the same as that of EP process, proving that individual carbon sphere had no catalysis function on H_2O_2 and O_3 . And only 6% phenol was adsorbed by the CS. Considering that Fe^{2+} played a key role in catalyzing H_2O_2 and O_3 , the same amount of Fe^{2+} (1.61 mg/L) as the total iron dissolution was added. The phenol degradation in 30 min and its k changed to 97.2% and 0.098 min^{-1} , demonstrating that the effects of homogeneous

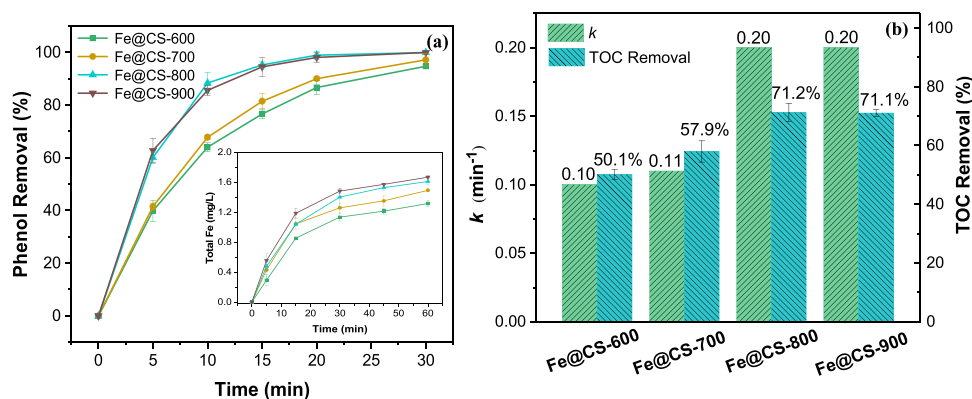


Fig. 3. The effect of calcination temperature on (a) Phenol degradation and Fe dissolution; (b) k value and TOC removal. Conditions: $T = 293$ K; stirring speed = 400 rpm; initial pH = 5.8; [phenol] = 100 mg/L; [catalyst] = 0.2 g/L; $I = 50$ mA; in-gas O_3 concentration = 55 mg/L, gas flow = 25 mL min⁻¹.

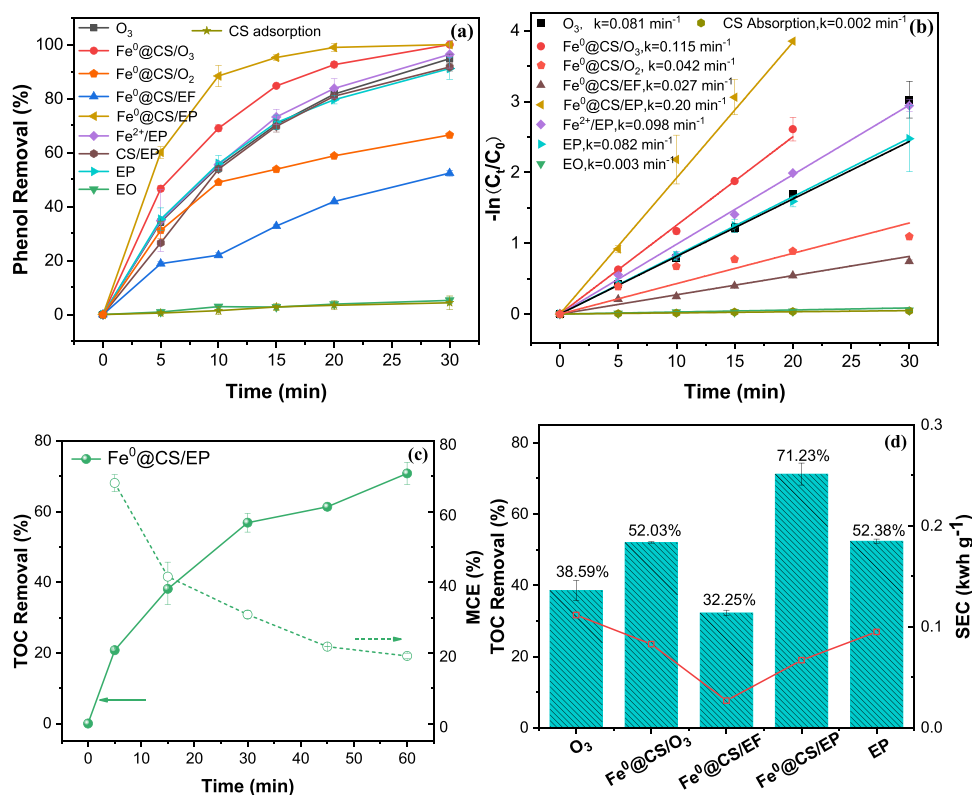


Fig. 4. (a) Phenol degradation and (b) Kinetic plots in various processes; (c) TOC removal and MCE for the Fe⁰@CS/EP process; (d) TOC removal at 60 min and SEC in various processes. Conditions: $T = 293$ K; stirring speed = 400 rpm; initial pH = 5.8; [phenol] = 100 mg/L; [catalyst] = 0.2 g/L; $I = 50$ mA; in-gas O_3 concentration = 55 mg/L, flow rate = 25 mL min⁻¹.

catalytic reactions might not be dominant. Surprisingly, the addition of Fe⁰@CS in EP accelerated the phenol degradation notably, with 100% removal within 15 min and k of 0.20 min⁻¹ in Fe⁰@CS/EP, which was 1.47, 0.74 and 6.41-folds higher than that of EP (0.082 min⁻¹), Fe⁰@CS/O₃ (0.115 min⁻¹) and Fe⁰@CS/EF (0.027 min⁻¹), respectively. According to Eq. (8), the synergism between Fe⁰@CS/O₂ and EP of the Fe⁰@CS/EP system were further assessed. Accordingly, the SF was calculated to be 1.61, revealing the significant synergistic effect of coupling Fe⁰@CS, O₃ and H₂O₂ for decontamination of phenol, which was attributed to the simultaneous catalysis of O₃ and H₂O₂ by Fe⁰@CS.

The mineralization of organics was also an important factor for evaluating the oxidation performance of AOPs. According to Fig. 4c, the TOC removal was 0.76% and 2.33% by EO and adsorption at 60 min. And ozonation (38.59%) processed a relatively high phenol

mineralization. Notably, the TOC removal of the composite processes performed better, 52.03% for Fe⁰@CS/O₃, 32.25% for Fe⁰@CS/EF, 52.38% for EP, and 71.23% for Fe⁰@CS/EP at 60 min (Fig. 4d). Meanwhile, within the reaction from 5 min to 60 min, MCE ranged from 70% to 20% of the Fe⁰@CS/EP process due to the reduced total organic carbon concentration (Fig. 4c). Energy consumption is also an important index in water treatment. As shown in Fig. 4d, the SEC of Fe⁰@CS/EP process was 0.067 kWh (g TOC)⁻¹, lower than those of EP (0.093 kWh (g TOC)⁻¹), Fe⁰@CS/O₃ (0.083 kWh (g TOC)⁻¹), and O₃ (0.112 kWh (g TOC)⁻¹). And the SEC value of Fe⁰@CS/EF was 0.027 kWh (g TOC)⁻¹ with an unsatisfactory mineralization (32.25%). Therefore, the addition of Fe⁰@CS to the EP process decreased SEC by 0.026 kWh (g TOC)⁻¹, along with the enhancement of mineralization (20.0%).

Many researchers have investigated the EP process by adding

heterogeneous catalyst or modifying cathode material, as well as the application of Fe⁰-based carbon catalysts to the hetero-catalytic O₃ or H₂O₂ process. As listed in Table 1, the Fe⁰@CS/EP process exhibited an excellent performance with the high mineralization efficiency of 100 mg/L phenol (71.2%, 60 min), low Fe dissolution (1.61 mg/L) and EEC (0.067 kWh (g TOC)⁻¹), and the TOF value of Fe⁰@CS as high as 1.005 L g⁻¹ min⁻¹ at initial pH 5.8. Compared with the reported EP process based PAN-CF/DSA and Carbon-PTFE/Pt, the addition of Fe⁰@CS significantly reduced the energy consumption by 0.113 and 0.383 kWh (g TOC)⁻¹, about 1.68 and 5.72 folds, separately [48,49]. Although some synthesized catalysts such as CuSi-BM₆₀, CMC etc. were dedicated to the catalytic EP process and promoted the degradation and mineralization of pollutants, the energy consumption of catalytic EP were 0.32 and 0.47 kWh (g TOC)⁻¹, still much higher than that of this study [8,13,50]. Besides, in relation to combining electrolysis, Fe⁰ and O₃ using Pt as anode and cathode (no H₂O₂ production), the TOF value of Fe⁰@CS in this work was approximately 8.5 times that of Fe⁰ in E-Fe⁰-O₃ [32]. Furthermore, the energy consumption was also dropped by 14.8 folds from 0.99 kWh (g TOC)⁻¹ (E-Fe⁰-O₃) to 0.067 kWh (g TOC)⁻¹. This result once again indicated the superiority of catalytic O₃ and H₂O₂ concurrently. Further comparison with the catalytic O₃ or H₂O₂ based carbonaceous Fe⁰ material, the Fe⁰@CS/EP process realized the faster degradation and mineralization of pollutants with a relatively lower iron dissolution and energy consumption [19,22,51]. Hence, Fe⁰@CS was an ultra-efficient and eco-friendly heterocatalyst to strengthen EP process by the simultaneous catalysis of O₃ and H₂O₂.

3.4. Operational parameters

The effects of current, catalyst dosage and initial pH on the Fe⁰@CS/EP process were investigated. When the current was 25.0, 50.0, 75.0, and 100.0 mA, the phenol degradation efficiency were 95.6%, 100.0%, 100.0% and 90.0% at 20 min, respectively (Fig. 5a), and the *k* values were 0.11, 0.20, 0.18, and 0.16 min⁻¹, respectively. Accordingly, the TOC removal was the highest of 71.2% at 50 mA, and then decreased ranged from 50 to 100 mA. This result could be rationalized because

more H₂O₂ was produced as the current increased, which was beneficial to drive peroxone and Fenton-like (Fe⁰@CS/EP) reaction. Nevertheless, excess H₂O₂ would quench •OH, leading to poor pollutant removal [52]. So the current of 50.0 mA was optimal.

As shown in Fig. 5b, phenol was completely removed within 30 min with catalyst dosage from 100.0 to 400.0 mg/L, but *k* value and total dissolved iron ranged with 0.16 – 0.20 min⁻¹ and 1.11 – 2.80 mg/L, respectively. And the *k* value reached maximum due to the sufficient active sites for activating O₃ and H₂O₂ when the catalyst dosage was 200.0 mg/L. The descending phenol degradation with catalyst dosage from 200 to 400 mg/L was possibly because the excess catalyst hindered the mass transfer of O₃ and H₂O₂ [33].

The effect of pH on EP and Fe⁰@CS/EP were compared (Figs. 5c and 5d), proving that the Fe⁰@CS/EP process performed better under pH 3.0 – 10.0. The degradation and mineralization efficiency of phenol in both processes increased first and then decreased obviously with the increasing pH. In terms of EP process, at pH 7, the phenol degradation at 30 min and its *k* value, as well as the TOC removal at 60 min were optimal, which were 100%, 0.16 min⁻¹ and 52.95%, respectively. When the initial pH was lower than 7.0, the increasing concentration of H⁺ might limit the amount of HO₂, which determined the chain reaction of producing •OH such as Eqs. (18–23). Under alkaline condition (pH = 10.0), the dissociation of O₃ and H₂O₂ to H₂O might be critically inhibited the removal rate. Therefore, phenol degradation and mineralization were the highest at pH 7 in EP. Contrastively, a better degradation and mineralization of phenol in Fe⁰@CS/EP was achieved than those in EP, which was due to the dual catalytic O₃ and H₂O₂ function of ≡Fe²⁺ generated from Fe⁰ corrosion in presence of O₃ and H₂O₂. The pK_a of phenol was 9.5 [53]. With the increase of pH from 3.0 to 10.0, phenol was gradually deprotonated. The *k* value of phenol degradation within 30 min and TOC removal within 60 min increased from 0.13 min⁻¹ and 49.4% to 0.20 min⁻¹ and 74.5% with increasing pH from 3.0 to 7.0, respectively [50]. The pH_{PZC} of Fe⁰@CS was 7.6, therefore, its surface hydroxyl groups were protonated when pH < 7.6, which had a strong attraction with O₃ and H₂O₂, and then accelerated the decomposition of O₃ and H₂O₂ into •OH. Moreover, the increase of

Table 1

Comparative studies on the EP, catalytic-EP and Hetero-catalytic O₃ or H₂O₂-based Fe⁰ processes in literatures.

Process	Cathode/ Anode	Catalyst (g L ⁻¹)	Experimental conditions	Pollutant removal	TOC removal	TOF (L g ⁻¹ min ⁻¹)	Total Fe (mg/L)	EEC (kwh (g TOC) ⁻¹)	Ref.
Fe ⁰ @CS/ EP	CB-PTFE/ DSA	0.2	100 mg/L phenol, V 250 mL, 55 mg/L O ₃ , I 50 mA, pH 5.8	100%, 20 min	71.2%, 60 min	1.005	1.61	0.067	This work
PAN-CF /DSA	–	–	200 mg/L phenol, V 1 L, 90 mg/L O ₃ , I 400 mA	100%, - 120 min	99%, –	–	–	0.18	[48]
EP	CB-PTFE/Pt	–	527.29 mg/L AR88, V 1 L, 30 mg/L O ₃ , I 700 mA, pH 7.35	95.4%, - –	70%, –	–	–	0.45	[49]
CuSi-BM ₆₀ /EP	CB-PTFE/SS	0.2	TC 10 mg/L, V 500 mL, 7.5 mg/L O ₃ , I 30 mA, pH 5.1	100%, 20 min	73.2%, 60 min	–	–	0.32	[50]
CuFe ₂ O ₄ / CNTs/EP	CNTs-PTFE GDE/Pt	0.2	20 mg/L FLU, V 100 mL, 14.5 mg/L O ₃ , I density 20 mA/cm ²	89%, 10 min	–	1.009	0.07	–	[13]
Self- circulating EP	CMC/Pt	–	20 mg/L ENR, NOR, OFL; V 400 mL, 40.2 mg/L O ₃ , current density 30 mA/cm ² , pH 4.2	90%, 10 min	79%, 2 h	–	–	0.47	[8]
E-Fe ⁰ -O ₃	Pt/Pt	1.0	0.19 mM NB, V 250 mL, 5.0 mg/L O ₃ , I 200 mA, pH 5.3	90.5%, 20 min;	85.2%, 120 min	0.118	1.3	0.99	[32]
mFe ⁰ /O ₃	–	40	500 mg/L <i>p</i> -NP, V 300 mL, 7.6 mg/L O ₃ , pH 5.3	100%, - –	89.5%*, 1 h	0.003	231	0.147	[19]
Fe@C-ATA/ H ₂ O ₂	–	0.5	50 mL 20 mg/L SMT, 40 mM H ₂ O ₂ , pH 4	95%, 10 min	96.8%, 400 min	0.063	0.72	–	[22]
MIL-88A-Fe ⁰ / H ₂ O ₂	–	0.1	20 mg/L AMX, V 100 mL, 5 mM H ₂ O ₂ , pH 4.0	100%, 60 min	60.4%, 90 min	0.931	2.545	–	[51]

Note: PAN-CF, polyacrylonitrile carbon fibre; SS, stainless steel; CMC, CoFe₂O₄/carbonized-MIL-100 (Fe); AR88, acid red 88; TC, tetracycline; ENR, enrofloxacin; NOR, norfloxacin; OFL, ofloxacin; NB, nitrobenzene; MB, methylene blue; *p*-NP, *p*-nitrophenol; CBZ, carbamazepine; SMT, sulfamethazine; AMX, amoxicillin; E-Fe⁰-O₃, a process combining electrolysis, Fe⁰, and O₃; mFe⁰/O₃, a micro-size Fe⁰/O₃; Fe@C-ATA, Fe-aminoterephthalic acid (Fe-ATA) complex as starting materials to synthesize Fe@C, MIL-88A-Fe⁰, Metal-organic frameworks (MOFs) derived zero-valent iron embedded in the carbon matrix structure; *COD removal.

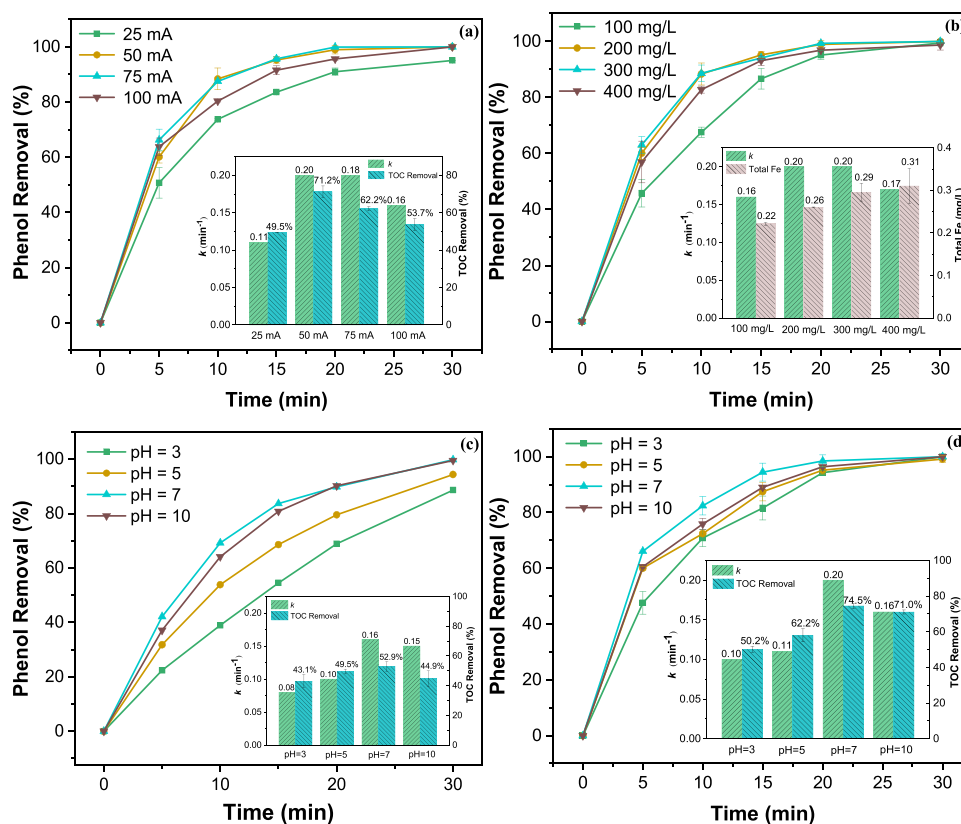
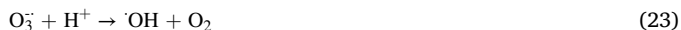


Fig. 5. Effect of (a) initial current; (b) catalyst dosage; (c) initial pH on the EP and (d) Fe⁰@CS/EP process. The inset patterns showed the TOC removal and total iron dissolution at 60 min. Except for the investigated parameter, other parameters were set as follows: T = 293 K; stirring speed = 400 rpm; initial pH = 5.8; [phenol] = 100 mg/L; [catalyst] = 0.2 g/L; I = 50 mA; in-gas O₃ concentration = 55 mg/L, flow rate = 25 mL min⁻¹.

pH was conducive to the ionization of phenol, and some ionized phenol tended to be adsorbed and degraded by the protonated Fe⁰@CS. Therefore, with the increase of pH, the degradation efficiency of phenol increased. However, when pH was up to 10, the k value and TOC removal decreased to 0.16 min⁻¹ and 71.0%, which could be ascribed to the negative effect of deprotonated surface of Fe⁰@CS on the ionized phenol adsorption. What's more, the increase of solution pH led to surface passivation of Fe⁰ and the stronger side reaction of O₃ and H₂O₂ to H₂O at higher pH value [43,46,50]. In brief, Fe⁰@CS/EP achieved excellent catalytic activity in a wide pH range (3.0 – 10.0).



3.5. Mechanism discussion

3.5.1. Identification of major ROS

In order to clarify the roles of ROS on phenol degradation in Fe⁰@CS/EP, the capture experiments were conducted by adding excess tert-butanol (TBA) and isopropanol (IPA) ($\cdot\text{OH}$ scavenger), superoxide dismutase (SOD, $\cdot\text{O}_2^-$ scavenger) [16], furfuryl alcohol (FFA, $^1\text{O}_2$ scavenger) as scavengers. As shown in Fig. 6a, the phenol degradation was largely depressed after the addition of TBA and IPA, revealing the

pivotal role of $\cdot\text{OH}$ on the degradation of phenol. Interestingly, the degradation rates of phenol also decreased after adding SOD, FFA and CAT, indicating that $\cdot\text{O}_2^-$, $^1\text{O}_2$ and H₂O₂ were also involved in Fe⁰@CS/EP. And the observed k decreased from 0.20 min⁻¹ to 0.19 min⁻¹, 0.05 min⁻¹ and 0.11 min⁻¹, respectively. To preferably manifest the contribution of different active species for phenol degradation, the inhibitory efficiency (η) of different scavengers were estimated through Eq. (24) [16].

$$\eta = (1 - k_s/k_0) \times 100\% \quad (24)$$

where k_0 is the degradation rate constant in the absence of scavengers, and k_s is the degradation rate constant in the presence of scavengers. As seen from Fig. 6b, the inhibitory efficiency of SOD was only 5%, indicating that $\cdot\text{O}_2^-$ made little contribution to the phenol degradation in Fe⁰@CS/EP. Moreover, the inhibition rate of TBA, IPA, FFA and CAT were found to be 85%, 90%, 75% and 45%, respectively. Therefore, $\cdot\text{OH}$ played a leading role in Fe⁰@CS/EP. Compared with three ROS inhibitors, the inferior inhibition efficiency of CAT revealed that although the generated H₂O₂ was devoted to Fe⁰@CS/EP and peroxone reactions, there was also catalytic ozonation (Fe⁰@CS/O₃) reaction for phenol degradation in Fe⁰@CS/EP.

Fig. 6c presented the $\cdot\text{OH}$ accumulation during 60 min of different processes. The $\cdot\text{OH}$ concentration was 10 μM in O₃ and EO, but 130.4 μM in Fe⁰@CS/EP, which was higher than that of the sum of Fe⁰@CS/O₃ (33.5 μM), Fe⁰@CS/EP (14.1 μM), and EP (50.5 μM) process, verifying that Fe⁰@CS significantly promoted the simultaneous decomposition of O₃ and H₂O₂ into $\cdot\text{OH}$ in Fe⁰@CS/EP. And the $\cdot\text{OH}$ concentration in Fe⁰@CS/O₂ was 9.8 μM , proving the existence of Fenton-like reaction due to the reduction of oxygen by Fe⁰. To further prove the promotion of $\cdot\text{OH}$ in Fe⁰@CS/EP, the ROS of different processes were also analysed by EPR. As shown in Fig. 6d, the intensity of

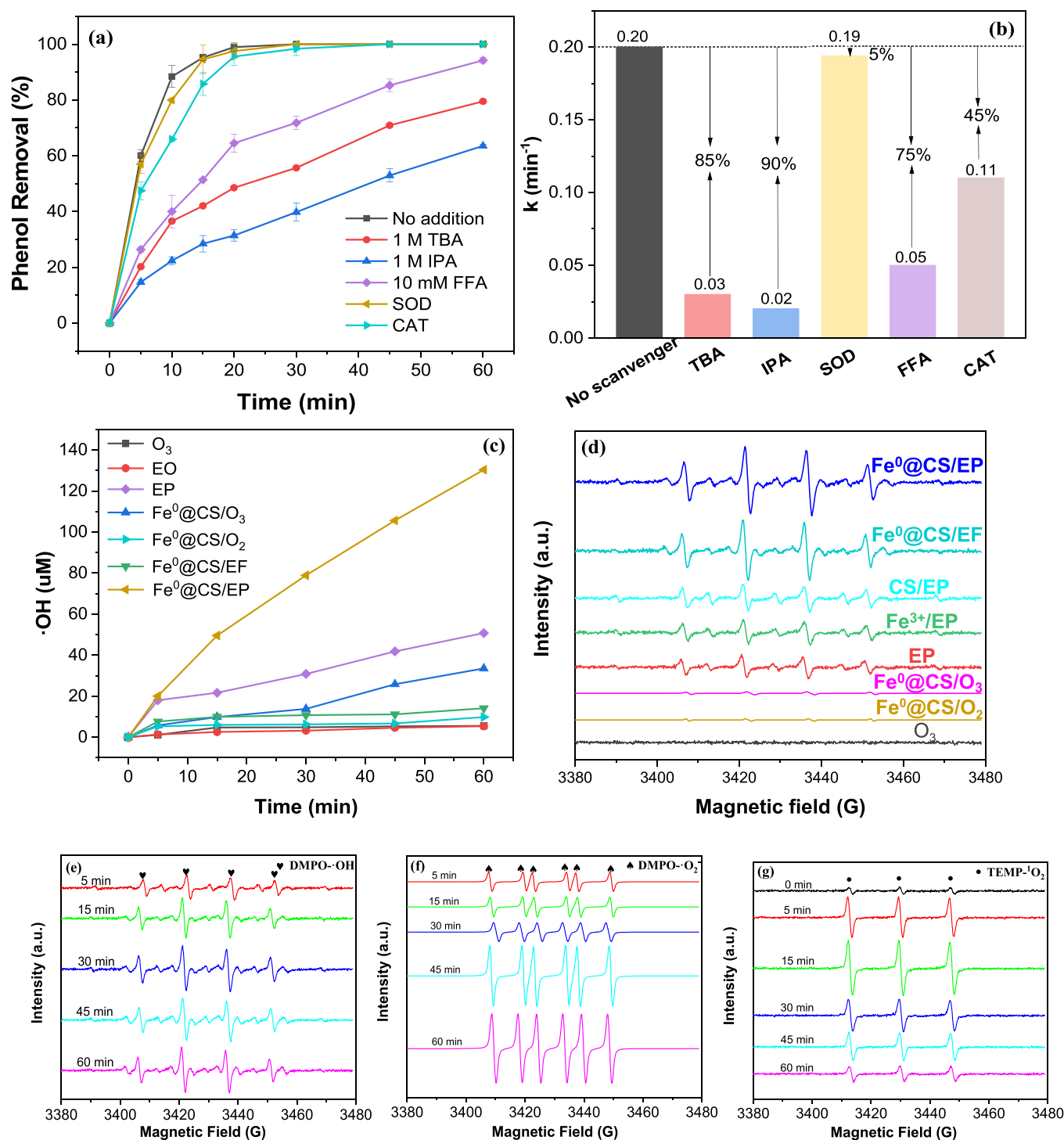


Fig. 6. (a) Phenol degradation and (b) its k with the addition of different scavengers in $\text{Fe}^0\text{@CS/EP}$; (c) The accumulated $\cdot\text{OH}$ concentration and (d) EPR spectra of $\text{DMPO}\cdot\text{OH}$ under different processes; (e-g) The EPR spectra of $\text{DMPO}\cdot\text{OH}$, $\text{DMPO}\cdot\text{O}_2$ and $\text{TEMP}\cdot\text{O}_2$ under different reaction time in $\text{Fe}^0\text{@CS/EP}$. Conditions: initial pH = 5.8; [phenol] = 100 mg/L; [catalyst] = 0.2 g/L; I = 50 mA; in-gas O_3 concentration = 55 mg/L; flow rate = 25 mL min^{-1} ; TBA = IPA = 1 M; FFA = 10 mM; SOD \geq 500 U/mL; CAT \geq 500 U/mL.

$\text{DMPO}\cdot\text{OH}$ in $\text{Fe}^0\text{@CS/EP}$ was the greatest compared with other processes. To study the mutual transformation process of ROS involved in $\text{Fe}^0\text{@CS/EP}$, the EPR test of different reaction time were carried out. The signals of $\text{DMPO}\cdot\text{OH}$, $\text{DMPO}\cdot\text{O}_2$ and $\text{TEMP}\cdot\text{O}_2$ were observed at 5 min, and the signals of $\text{DMPO}\cdot\text{OH}$ and $\text{DMPO}\cdot\text{O}_2$ were gradually strengthened during the reaction, while the signal of $\text{TEMP}\cdot\text{O}_2$ showed an obvious increase in the first 15 min and decreased from 15 min to 60 min in $\text{Fe}^0\text{@CS/EP}$. It was speculated that O_2 was transformed into

$\cdot\text{OH}$ or $\cdot\text{O}_2$ in the later 15 min. Since EP, $\text{Fe}^0\text{@CS/O}_3$ and $\text{Fe}^0\text{@CS/EF}$ were the main reactions, ROS generation were also investigated by EPR to reveal the source of ROS in $\text{Fe}^0\text{@CS/EP}$. As indicated in Fig. S8a-8c, the signals of $\text{DMPO}\cdot\text{OH}$ and $\text{TEMP}\cdot\text{O}_2$ at 5 min in EP were observed, and increased slightly with the progress of the reaction. No $\text{DMPO}\cdot\text{O}_2$ appeared in EP. Similarly, the signals of $\text{DMPO}\cdot\text{OH}$, $\text{DMPO}\cdot\text{O}_2$ and $\text{TEMP}\cdot\text{O}_2$ were also observed in $\text{Fe}^0\text{@CS/EF}$ and $\text{Fe}^0\text{@CS/O}_2$ (Fig. S9d-9f and Fig. S9j-9l). Both of the $\text{DMPO}\cdot\text{OH}$ signals increased at the

initial 15 min and remained unchanged thereafter. The signals of DMPO- $\cdot\text{O}_2$ appeared at 5 min and obviously increased with the reaction. However, the signals of TEMP- $^1\text{O}_2$ in $\text{Fe}^0\text{@CS/EP}$ and $\text{Fe}^0\text{@CS/O}_2$ increased in the first 15 or 30 min and then decreased, which was probably attributed to the decrease of the conversion of $^1\text{O}_2$ to $\cdot\text{O}_2$ because of the decline of pH with the reaction, resulting in the decrease of $^1\text{O}_2$ and increase of $\cdot\text{O}_2$ after 15 min. The identical ROS evolution also showed both the $\text{Fe}^0\text{@CS/O}_2$ and $\text{Fe}^0\text{@CS/EP}$ processes adhered to the reaction of $\text{Fe}^0\text{@CS}$ and H_2O_2 . There were the signals of DMPO- $\cdot\text{OH}$, DMPO- $\cdot\text{O}_2$ and TEMP- $^1\text{O}_2$ at 5 min in $\text{Fe}^0\text{@CS/O}_3$ (Fig. S9g–9i). Both signals of DMPO- $\cdot\text{OH}$ and DMPO- $\cdot\text{O}_2$ increased, and TEMP- $^1\text{O}_2$ almost remained unchanged with the reaction. $\cdot\text{O}_2$ in $\text{Fe}^0\text{@CS/O}_3$ originated from the reaction between $\text{Fe}^0\text{@CS}$ and H_2O_2 because H_2O_2 could be produced due to the reduction of dissolved oxygen by Fe^0 [19]. Therefore, the increase of $\cdot\text{OH}$ in $\text{Fe}^0\text{@CS/EP}$ was derived from the reactions of peroxone ($\text{O}_3/\text{H}_2\text{O}_2$), $\text{Fe}^0\text{@CS/H}_2\text{O}_2$ and $\text{Fe}^0\text{@CS/O}_3$. And $\cdot\text{O}_2$ was generated by the reaction of $\text{Fe}^0\text{@CS/H}_2\text{O}_2$. Besides, $^1\text{O}_2$ in $\text{Fe}^0\text{@CS/EP}$ was mainly from the process of $\text{Fe}^0\text{@CS/H}_2\text{O}_2$.

3.5.2. Quantitative evaluation the role of various reactions in $\text{Fe}^0\text{@CS/EP}$

When O_2 was sparged into the reaction during electrolysis, H_2O_2 was mainly generated continuously from the dissolved O_2 at the carbon-PTFE cathode. Therefore, catalytic ozonation, Fenton-like, peroxone reactions and direct molecule ozone reaction could be involved in $\text{Fe}^0\text{@CS/EP}$ process due to the interaction among $\equiv\text{Fe}^{2+}/\equiv\text{Fe}^{3+}$ from iron corrosion, generated H_2O_2 and aerated O_3 . Therefore, it is necessary to quantitatively analyze the contributions of these reactions to shed light on the mechanisms for phenol degradation and mineralization in $\text{Fe}^0\text{@CS/EP}$.

In this study, the proportion of pseudo-first-order rate constant (k) of each reaction in the whole $\text{Fe}^0\text{@CS/EP}$ process ($k = 0.20 \text{ min}^{-1}$) was used to evaluate the contribution of these reactions. First of all, the

contribution of adsorption and EO to phenol removal in $\text{Fe}^0\text{@CS/EP}$ was represented by the removal rate since the adsorption and EO was the sole involved-reaction. The k of phenol removal in adsorption and EO were 0.002 min^{-1} and 0.003 min^{-1} , respectively (Fig. S3). Therefore, it can be calculated that the contribution of adsorption and EO were 1.0% and 1.5% in $\text{Fe}^0\text{@CS/EP}$. Subsequently, the contribution of direct molecule ozone reaction could be calculated by the rest proportion of excluding $\cdot\text{OH}$ (90.0%), adsorption (1.0%) and EO (1.5%) in $\text{Fe}^0\text{@CS/EP}$, i.e., 7.5%. Moreover, $\cdot\text{OH}$ was mainly generated by catalytic ozonation, Fenton-like and peroxone reaction. To calculate the contribution of catalytic ozonation, excess catalase (CAT, H_2O_2 scavenger) was added. It was well-known that H_2O_2 was involved in Fenton-like and peroxone reactions. As shown in Figs. 6a and 6b, phenol degradation was largely depressed without H_2O_2 , and the k was declined to 0.11 min^{-1} , which demonstrated that the contribution of catalytic ozonation, direct molecule ozone reaction, adsorption and electro-oxidation were about 55.0%, and then the contribution of catalytic ozonation reaction was about 45.0% (= 55.0–10.0%). Considering that the supply of H_2O_2 was sufficient, the contribution of Fenton-like reaction was calculated by the k of phenol removal in $\text{Fe}^0\text{@CS/EP}$ (0.027 min^{-1}). Thus, the contribution of Fenton-like reaction was about 13.5%. Subsequently, the contribution of peroxone was about 39.0% (= 100.0–13.5% of Fenton-like reaction - 45.0% of catalytic ozonation - 7.5% of direct molecule O_3 - 1.0% of adsorption - 1.5% of EO).

3.5.3. O_3 and H_2O_2 utilization

Considering O_3 and H_2O_2 were important active species for $\cdot\text{OH}$ formation, their concentration were measured during the reaction, respectively. As shown in Figs. 7a and 7b, the in-gas O_3 was constant at 55 mg/L. The order of aqueous O_3 and off-gas O_3 concentration in different processes were as follows: $\text{O}_3 > \text{EP} > \text{Fe}^0\text{@CS/O}_3 > \text{Fe}^0\text{@CS/EP}$. The aqueous O_3 and off-gas O_3 concentration increased with the

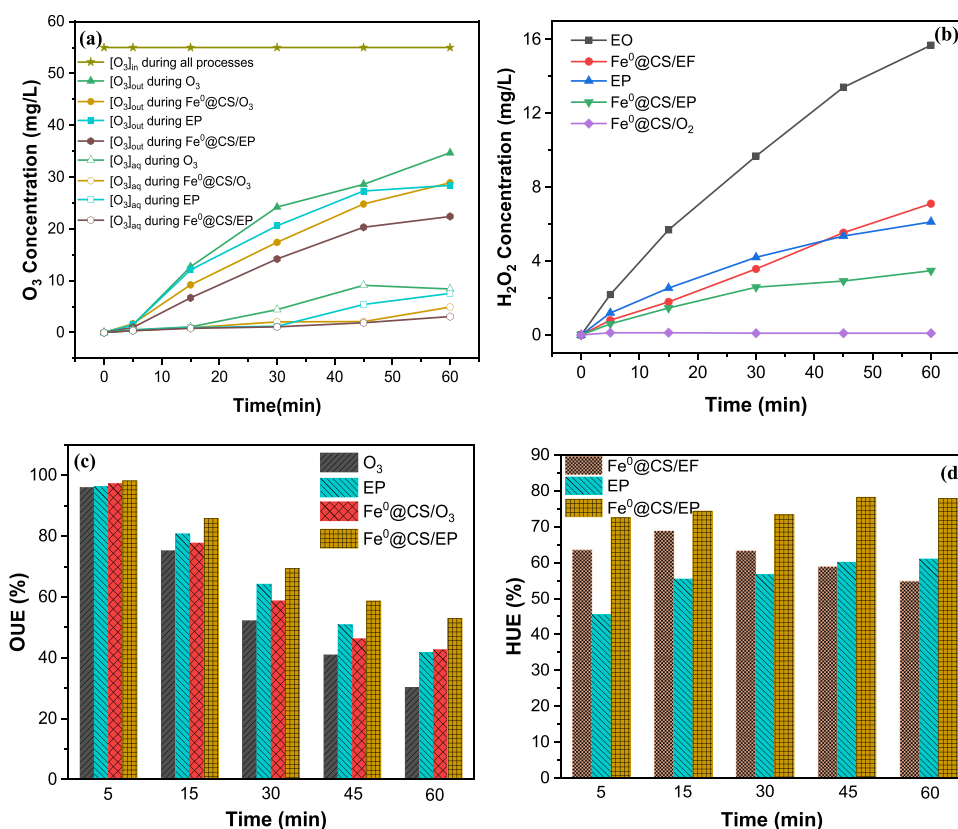


Fig. 7. (a) The variation of aqueous and off-gas O_3 and (b) aqueous H_2O_2 ; (c) OUE and (d) HUE in various processes. Conditions: initial pH = 5.8; [catalyst] = 0.2 g/L; T = 293 K; stirring speed = 400 rpm; [phenol] = 100 mg/L; I = 50 mA; in-gas O_3 concentration = 55 mg/L, gas flow = 25 mL min^{-1} .

reaction and their values at 60 min in O₃, EP, Fe⁰@CS/O₃ and Fe⁰@CS/EP were 8.38 mg/L and 34.7 mg/L, 7.54 mg/L and 28.4 mg/L, 4.91 mg/L and 28.9 mg/L, 3.06 mg/L and 22.4 mg/L, proving that both H₂O₂ and Fe⁰@CS could promote ozone decomposition. Concurrently, H₂O₂ production and was accumulated to 15.68 mg/L during 60 min in EO, and displayed the order of EO (15.68 mg/L) > EP (7.10 mg/L) > Fe⁰@CS/EP (6.12 mg/L) > Fe⁰@CS/O₃ (3.47 mg/L). And H₂O₂ residue was very low (0.09 mg/L) at 60 min in Fe⁰@CS/O₂. Therefore, it was negligible for the calculation of HUE. These result further illustrated that O₃ and H₂O₂ could consume each other, and Fe⁰@CS also promoted the decomposition of H₂O₂. The lowest concentration of O₃ and H₂O₂ in Fe⁰@CS/EP verified Fe⁰@CS could catalyze O₃ and H₂O₂ simultaneously.

As indicated in Figs. 7c and 7d, OUE and HUE were further calculated. OUE at 5 min in O₃ and Fe⁰@CS/O₃ were 97.28% and 95.98%, respectively. It was noted that a larger amount of O₃ was consumed by the high concentration of phenol in the initial reaction. Therefore, OUE gradually decreased due to the abatement of organic matters with the reaction process. At 60 min, OUE in O₃ and Fe⁰@CS/O₃ were 30% and 42.63%, which indicated Fe⁰@CS could effectively promote O₃ decomposition. On the other hand, HUE in Fe⁰@CS/EP increased from 63.38% at 5 min to 68.65% at 15 min, and then decreased to 55.0% at 60 min because Fe⁰ inner carbon spheres was first oxidized to $\equiv\text{Fe}^{2+}$, and then gradually oxidized to $\equiv\text{Fe}^{3+}$. OUE in both EP and Fe⁰@CS/EP at 5 min were corresponded to 96.0% and 98.2%. As the reaction proceeded, OUE in Fe⁰@CS/EP was 53.0%, still higher than that of EP (41.7%) at 60 min. Moreover, HUE in EP was between 45.4% at 5 min and 60.9% at 60 min. The index of Fe⁰@CS/EP showed a similar increasing trend, ranging from 72.5% at 5 min to 77.8% at 60 min. The OUE and HUE in Fe⁰@CS/EP process increased by 1.9–11.5% and 16.8–27.1% in contrast to EP, respectively, which further certificated Fe⁰@CS could accelerate the decomposition of O₃ and H₂O₂ simultaneously, resulting in the augmented performance for the pollutant degradation and mineralization.

3.5.4. Analysis of the used Fe⁰@CS in different systems

In order to investigate the mechanism of simultaneous catalysis in Fe⁰@CS/EP, SEM, XRD and XPS of used Fe⁰@CS after five cycles in Fe⁰@CS/O₃, Fe⁰@CS/EP and Fe⁰@CS/EP were characterized, respectively. From Fig. 8a, the least corrosion particles appeared on the surface of the reacted Fe⁰@CS in O₃. By contrast, more corrosion product was observed on the surface of the reacted Fe⁰@CS in EP and EP. It was inferred that H₂O₂ has a stronger ability to corrode Fe⁰-embedded in carbon sphere than O₃ because the electrophilic O₃ was more easily adsorbed on the surface of the defective carbon sphere (Raman results) [54]. To further compare the corrosion effects of O₃ and H₂O₂ on Fe⁰@CS, Tafel in O₃, H₂O₂ and both coexist were tested, respectively (Fig. 8b). The potential of Fe⁰@CS in O₃ was 0.42 V, which was obviously higher than that in H₂O₂ (0.07 V), indicating the corrosion rate of Fe⁰@CS faster in H₂O₂ than that in O₃. Concurrently, the potential of Fe⁰@CS in O₃ and H₂O₂ was 0.41 V, which was near the corrosion potential in H₂O₂. Therefore, when O₃ and H₂O₂ coexisted, the corrosion of H₂O₂ to Fe⁰ embedded in carbon sphere was dominant.

The XRD pattern of fresh and used Fe⁰@CS (Fig. 8c) displayed all samples had a broad diffraction peak of graphite carbon (002) at 23°, indicating the structural stability of carbon sphere under strong oxidant environment [40]. The unreacted Fe⁰@CS showed obvious peaks at 44.6°, 65.0°, and 82.4°, which were corresponded to the pattern of standard Fe⁰ [31]. After reaction, the characteristic peaks of Fe₃O₄ appeared in Fe⁰@CS/EP, Fe⁰@CS/O₃ and Fe⁰@CS/EP processes. According to the intensity of Fe⁰ diffraction peak, Fe⁰@CS corrosion followed the sequence: Fe⁰@CS/EP > Fe⁰@CS/EP > Fe⁰@CS/O₃, which also confirmed that H₂O₂ processed a stronger ability than O₃ to corrode Fe⁰ embedded in carbon sphere. As seen from Fig. S10, the TOC removal in Fe⁰@CS/EP was 18.97% at 5 min and 32.25% at 60 min, higher than that of 5 min (14.67%) and lower than that of 60 min (52.52%) in

Fe⁰@CS/O₃. Therefore, compared with H₂O₂, O₃ corroded Fe⁰ embedded in carbon sphere more slowly, leading to the inferior mineralization efficiency at initial 15 min. Nevertheless, phenol mineralization in Fe⁰@CS/EP were 20.76% and 70.8% at 5 min and 60 min, respectively. These phenomena further indicated Fe⁰@CS had synergistic effect on the catalysis of O₃ and H₂O₂, and H₂O₂ played a more important role in the corrosion of Fe⁰-embedded in carbon sphere during the Fe⁰@CS/EP process.

To further explore the catalytic mechanism, the functional groups on the surface of fresh and used Fe⁰@CS in different processes were further examined by XPS. C1s and O1s was obviously tested in the fullrange scan of fresh Fe⁰@CS (Fig. S12). However, C1s, O1s and Fe2p were observed in the fullrange scan of the used samples, suggesting that iron species was exposed to the surface of carbon sphere after the reaction. The C1s characteristic peaks (Fig. S13) of fresh Fe⁰@CS at C=O (carbonyl and carboxyl) bond (286.8 eV), C=C (285.3 eV), C-O (285.1 eV), and C-C (283.8 eV) accounted for 25.5%, 7.0%, 59.0%, and 8.5%, respectively [11]. O1s spectrum (Fig. 8d) of fresh Fe⁰@CS was deconvoluted into four peaks, including Fe-O (530.3 eV), -O (531.7 eV), O-C=C (533.3 eV) and O-C (532.6 eV), accounting for 6.2%, 71.23%, 9.3%, and 13.26%, respectively [8]. The presence of O-C=C and O-C improved the surface wettability of catalyst (Fig. S3), which was advantageous to the activation of aqueous reactants (O₃ and H₂O₂) at the catalytic interface.

Due to the embedding of carbon sphere, the intensity of Fe was weak on the surface of fresh Fe⁰@CS (Fig. 8e). This result was consistent with the result of full spectrum scanning. After reaction, the signals of Fe-O at 530.3 eV in Fe⁰@CS/EP (46.8%), Fe⁰@CS/O₃ (35.6%) and Fe⁰@CS/EP (25.9%) were significantly enhanced [8], which was ascribed to the corrosion of Fe⁰ and exposure of iron oxide on the surface of carbon spheres. Fe2p_{1/2} was obtained at 723.9 eV, Fe2p_{3/2} was found at 710.3 eV, and shake-up satellites were observed at 719.5 and 727.4 eV, suggesting that the splitting energy between Fe2p_{1/2} and Fe2p_{3/2} peaks was 13.6 eV and $\equiv\text{Fe}^{2+}$ existed in the reacted Fe⁰@CS. Besides, the other deconvoluted peaks at 711.4, 725.0, 713.7 and 732.2 eV proved the existence of $\equiv\text{Fe}^{3+}$ on the surface of the reacted Fe⁰@CS [8]. Moreover, $\equiv\text{Fe}^{3+}$ exhibited an increased tendency with proportion with 59.0%, 61.4% and 65.8% while $\equiv\text{Fe}^{2+}$ decreased with 41.0%, 38.6% and 34.2% in Fe⁰@CS/EP, Fe⁰@CS/O₃ and Fe⁰@CS/EP, respectively. After reaction, $\equiv\text{Fe}^{2+}$ and $\equiv\text{Fe}^{3+}$ generated on the surface of reacted Fe⁰@CS due to the oxidation of O₃ or H₂O₂, which supported the XRD results. The highest component of $\equiv\text{Fe}^{2+}$ after Fe⁰@CS/EP was attributed to the activation of passive layer by H₂O₂ [46]. According to the highest content of $\equiv\text{Fe}^{3+}$ of Fe⁰@CS in Fe⁰@CS/EP, it was inferred that both O₃ and H₂O₂ could oxidized Fe⁰ into $\equiv\text{Fe}^{2+}$ for accelerating the decomposition of O₃ and H₂O₂ into ROS with the formation of $\equiv\text{Fe}^{3+}$, finally leading to highest proportion of $\equiv\text{Fe}^{3+}$ on the surface of reacted Fe⁰@CS.

3.5.5. Mechanism of Fe⁰@CS in heterogeneous EP

Based on the above analysis, the mechanism of Fe⁰@CS in catalytic EP was illustrated as a scheme in Fig. 9. There was a large amount of dissolved oxygen in the solution due to the continuous aeration of O₂/O₃ mixture-H₂O₂ could be generated from 2-electron oxygen reduction reaction of cathode (Eq. (25)) and the reduction of O₂ by Fe⁰ (Eq. (26)) in Fe⁰@CS/EP [46]. What's more, the generated H₂O₂ could strongly activate Fe⁰ into $\equiv\text{Fe}^{2+}$ through rapid corrosion of Fe⁰ (Eq. (27)) [46]. And then H₂O₂ was further transferred into $\cdot\text{OH}$ in the presence of the $\equiv\text{Fe}^{2+}$ catalysis, and $\equiv\text{Fe}^{3+}$ was generated simultaneously (Eq. (28)). In addition, H₂O₂ could also reduce $\equiv\text{Fe}^{3+}$ to $\equiv\text{Fe}^{2+}$, accompanied by the formation of $\cdot\text{O}_2^-$ (Eq. (29)) [22]. The electron transfer between $\equiv\text{Fe}^{3+}/\equiv\text{Fe}^{2+}$ accelerated the catalytic O₃ and H₂O₂. For $^1\text{O}_2$ generation, 2 molecular $\cdot\text{O}_2$ could react to form 2 molecular $^1\text{O}_2$ (Eq. (30)), which explained the existence of $^1\text{O}_2$ in the Fe⁰@CS/EP. On the other hand, O₃ was first adsorbed on the surface of defective carbonsphere and later reacted with inner Fe⁰ for the generation of $\equiv\text{Fe}^{2+}$ (Eq. (31)), which catalyzed O₃ into $\cdot\text{OH}$ (Eq. (32) and Eq. (33)). In addition, the

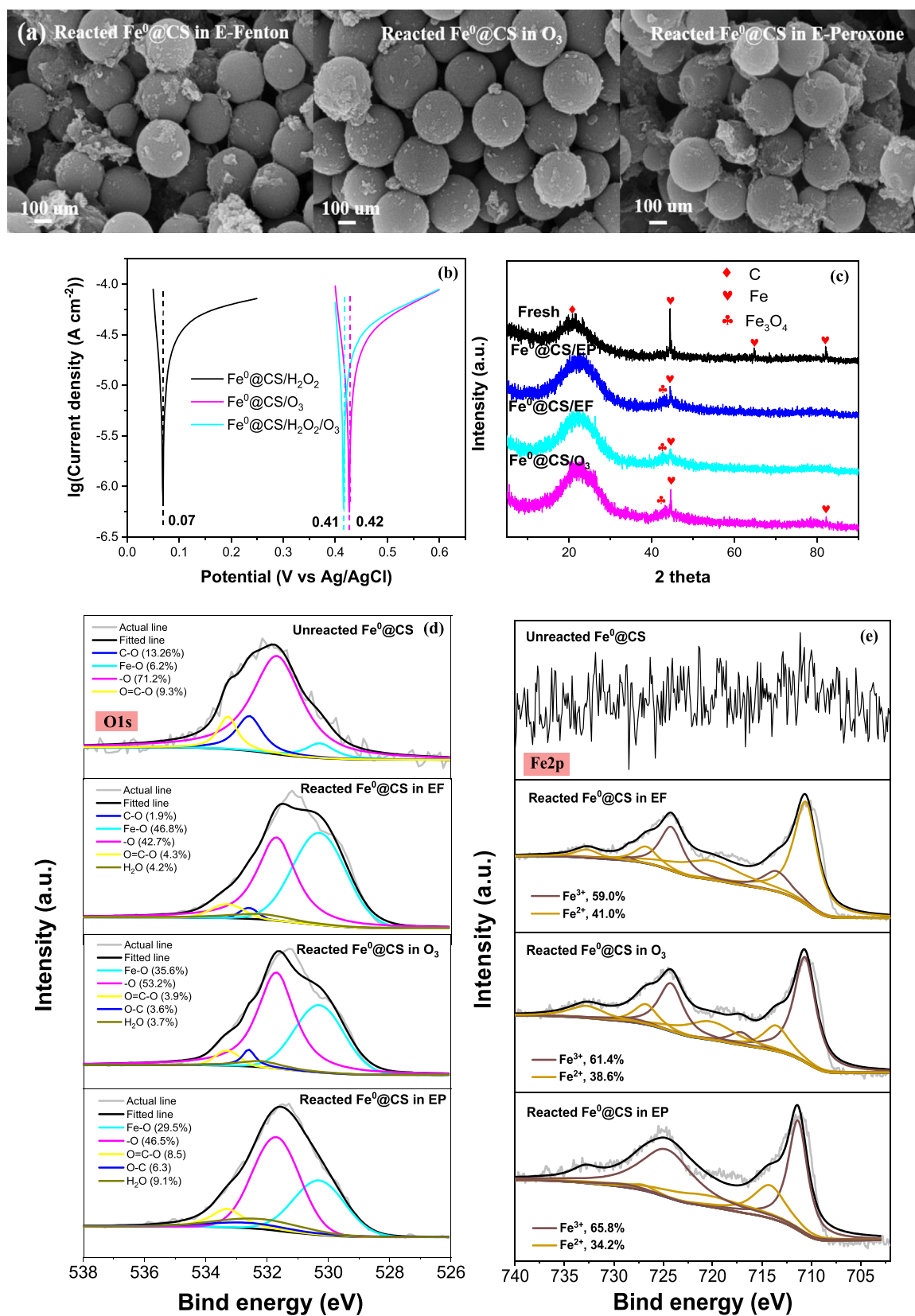


Fig. 8. (a) SEM of reacted $\text{Fe}^0\text{@CS}$; (b) Tafel polarization curves; (c) XRD; XPS spectral peaks of (d) O1s and (e) Fe2p of the fresh and reacted $\text{Fe}^0\text{@CS}$ in different processes.

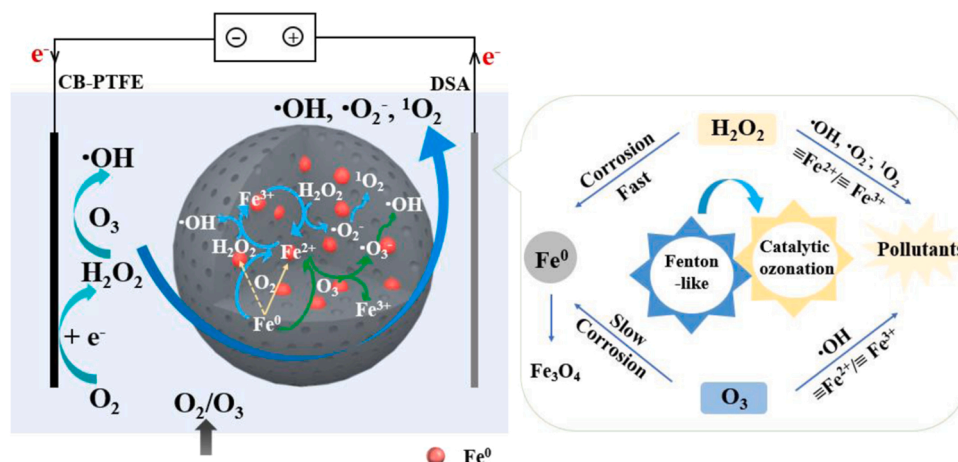
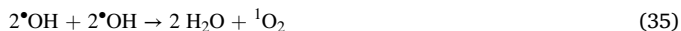
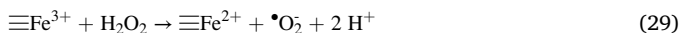
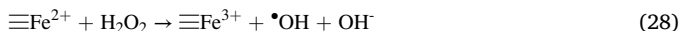
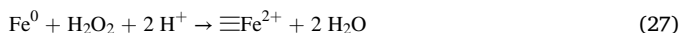


Fig. 9. Schematic mechanism of Fe⁰@CS in heterogeneous EP.

homogeneous peroxone reaction also occurred in solution, leading to the generation of $\bullet\text{OH}$ (Eq. (34)). And two $\bullet\text{OH}$ molecules would produce $^1\text{O}_2$ (Eq. (35)), which was consistent with the appearance of TEMP- $^1\text{O}_2$ signal in EP.

In summary, the catalytic effect of $\text{Fe}^0\text{@CS}$ on strengthening EP can be attributed to three effects: (1) Both O_3 and H_2O_2 could oxidize Fe^0 into $\equiv\text{Fe}^{2+}$, which further effectively catalyzed the formation of O_3 or H_2O_2 into $\cdot\text{OH}$ or $\cdot\text{OH}$, $\cdot\text{O}_2$ and $^1\text{O}_2$, respectively. (2) In coexistence of O_3 and H_2O_2 , the Fenton-like process accelerated the catalytic ozonation reaction due to the faster corrosion of H_2O_2 than O_3 to Fe^0 -encapsulated in carbon spheres. (3) In addition, the dissolved Fe^{2+} ions participated in catalyzing O_3 and H_2O_2 in the solution. Besides, the homogeneous reaction of $\text{O}_3/\text{H}_2\text{O}_2$ was also devoted to the pollutant removal. Heterogeneous catalysis played a major role for the accelerated degradation of phenol. It was speculated that H_2O_2 corrosion played a leading role in the formation of $\equiv\text{Fe}^{2+}$ in the catalytic EP process. In particular, the coating of carbon sphere protected Fe^0 from direct oxidation by O_3 and H_2O_2 and greatly reduced the total iron dissolution. And $\text{Fe}^0\text{@CS}$ with the porous spherical structure and large specific surface area increased the contact for O_3 and H_2O_2 molecules and effectively improved their mass transfer efficiency. Therefore, $\text{Fe}^0\text{@CS}$ manifested high activity in $\text{Fe}^0\text{@CS/EP}$.



as the multiple carboxylic acids such as adipic acid, fumaric acid, maleic acid, succinic acid, malonic acid, oxalic acid, formic acid and acetic acid in $\text{Fe}^0/\text{CS}/\text{EP}$ were detected. The possible pathways for phenol oxidation was proposed in Fig. S14. Firstly, $\bullet\text{OH}$ attacked the ortho, meta and para-positions on phenol and generated catechol, resorcinol and hydroquinone. Then, catechol and hydroquinone were further oxidized to 1,2-benzoquinone and 1,4-benzoquinone. According to report, resorcinol was hydroxylated by $\bullet\text{OH}$ to form 1,2,4-benzenetriol [55]. Then, the ring opening reaction of 1, 2-benzoquinone, 1, 2, 4-benzenetriol and 1, 4-benzoquinone happened and they were turned to various macromolecular carboxylic acids including adipic acid, fumaric acid, maleic acid, succinic acid and malonic acid. It was also speculated that adipic acid was the ring opening product of 1, 2-benzoquinone according to the fact that benzoquinone was almost completely converted, while a large amount of adipic acid appeared at 30 min (Fig. S15a). Furthermore, adipic acid was oxidized to maleic acid. After multiple oxidation reactions, these macromolecular carboxylic acids were further oxidized to oxalic acid, formic acid and acetic acid. Finally, oxalic acid, formic acid and acetic acid were mineralized to CO_2 and H_2O .

Figs. 10a and 10b presented the concentration of primary intermediates including catechol, resorcinol, hydroquinone and benzoquinone during the reaction of EP and $\text{Fe}^0/\text{CS}/\text{EP}$, revealing that the addition of Fe^0/CS could significantly reduce the accumulation of benzoquinone during the reaction, which was almost completely removed at 30 min. These substances were then further converted into various carboxylic acids. From Fig. S15a and S15b, compared with EP, the $\text{Fe}^0/\text{CS}/\text{EP}$ process accelerated the formation and mineralization of various carboxylic acids such as adipic acid, formic acid, acetic acid, fumaric acid, succinic acid, malonic acid, maleic acid and oxalic acid markedly. These carboxylic acids were further mineralized into CO_2 and H_2O . In terms of the $\text{Fe}^0/\text{CS}/\text{EP}$ process, there were 6.6 mg/L adipic acid and 7 mg/L maleic acid remained at 60 min.

The analysis of acute toxicity of the degradation intermediates was necessary. The EC_{50} is defined as the concentration of the tested compounds resulting in a 50% reduction of respiration rate of activated sludge. According to report, the toxicity of dihydroxybenzenes were higher than that of phenol ($EC_{50} = 2.67$ mg/L), and the EC_{50} of the main product hydroquinone was 0.5 mg/L [56]. Among all the compounds, benzoquinone was the most toxic one ($EC_{50} = 0.01$ mg/L). As is well-known that, for a biological process, EC_{50} of benzoquinone should not be lower than 3 mg/L. Therefore, it would be conservative to conclude that the wastewater will be suitable for biological treatment when the EC_{50} of the wastewater is below 3 mg/L [57]. Gratifyingly, dihydroxybenzenes and benzoquinone were degraded into various carboxylic acids completely after 30 min, and their toxicity was much less than that of phenol, reaching the level suitable for biological treatment

3.6. Phenol degradation pathway and the intermediates toxicity

As shown in Table S9, the intermediates including catechol, resorcinol, hydroquinone, 1,2-benzoquinone and 1,4-benzoquinone, as well

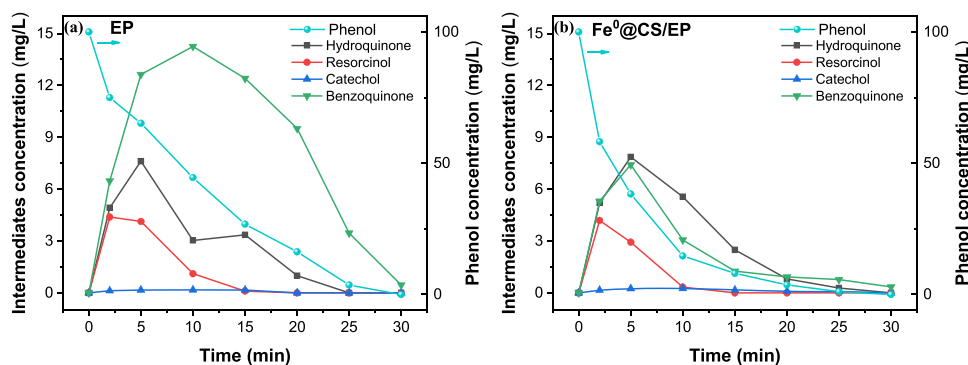


Fig. 10. The change of intermediates for phenol degradation in (a) EP and (b) Fe⁰@CS/EP process.

[57].

3.7. Catalyst stability and reusability

Cyclic experiments confirmed Fe⁰@CS maintained 100% of phenol removal within 30 min after five consecutive runs of Fe⁰@CS/EP process (Fig. 11a). However, k value and TOC removal showed a downward trend from 0.20 min⁻¹ and 71.2% to 0.13 min⁻¹ and 50.6% after five cycles (Fig. 11b). According to previous SEM and XPS results, this phenomenon was attributed to the continuous corrosion and oxidation of Fe⁰ by H₂O₂ and O₃, leading to a large amount of iron oxide deposited on the surface of carbon sphere. Meanwhile, iron ion was leaked into the solution, and the concentration of total Fe was 1.61, 1.31, 1.08, 0.82 and 0.60 mg/L, respectively, in five cycles. Justifiably, iron oxidation and dissolution resulted in the decline of phenol degradation and mineralization during the cyclic Fe⁰@CS/EP experiment. Even so, the iron content in the used catalysts was 3.22% by ICP-MS. The presence of considerable amount of iron in the sample after one use, further was proved to be Fe⁰ by XRD (Fig. S6), which endorsed its potential reusability. In previous work, the total Fe concentration were 231 and 2.545 mg/L in 60 min of the mFe⁰/O₃ and MIL-88A-Fe⁰/H₂O₂ processes [19,51]. Compared with those, the preparation of Fe⁰@CS significantly reduced the total iron dissolution in dual catalytic H₂O₂ and O₃ due to the protection of carbon sphere. Nevertheless, it should be pointed that Fe³⁺ observed in the solution due to the use of Fe⁰@CS during the degradation of phenol in Fe⁰@CS/EP will bring another environmental problem. Therefore, it is essential to remove Fe³⁺ from the final solution by adjusting solution pH to weak alkalinity (8–9) with coagulants such as CaCO₃, CaO, and Ca(OH)₂ or introducing adsorbents such as montmorillonite [58,59].

3.8. Environmental application

3.8.1. Degradation of phenol dissolved in real water, HA and various inorganic anions

In order to analyze the influence of the aqueous matrix on the degradation of the phenol by Fe⁰@CS/EP, four different aqueous matrices (tap water, coal reverse osmosis water from coal chemical plant in Hebei, secondary wastewater effluent from the reclaimed water station in Nankai University and lake water from mati-lake in Nankai University) were used (See Table S7 for water quality parameters). From Fig. 12a, it could be seen that the degradation efficiency of phenol followed the trend of coal reverse osmosis water < ultrapure water < tap water ≈ lake water ≈ secondary wastewater effluent. Proverbially, during ozonation, dissolved organic matter (DOM) can react directly with O₃ and act as promoters of radical chain reactions to promote O₃ decomposition. In contrast, carbonate/bicarbonate alkalinity has a stabilizing effect on O₃ decomposition by scavenging •OH and thus inhibiting the radical chain reactions. Therefore, O₃ stability usually increases with increasing carbonate/bicarbonate and decreases with increasing DOC of water matrix [60]. Therefore, the in-situ produced H₂O₂ during Fe⁰@CS/EP could enhance •OH exposures in tap water having high ozone stability due to its low DOM and high HCO₃⁻ (108 mg/L) contents, leading to the accelerated phenol degradation. In addition, the presence of Cl⁻ would promote the degradation of pollutants. Therefore, all of the electron-rich components of DOM, high concentration of HCO₃⁻ and Cl⁻ in the lake water and secondary effluent were conducive to phenol degradation. Nevertheless, a large amount of dissolved O₃-resistant oil substances competed with phenol for •OH, resulting in the descending degradation in the coal reverse osmosis water. Fortunately, the efficiency of phenol degradation still reached 100% in 20 min attributed to extremely high concentration of Cl⁻. These results indicated that the Fe⁰@CS/EP process had great potential in treating real water.

The effect of HA and various anions in real water on the removal of pollutants was further investigated in detail. According to Table S7,

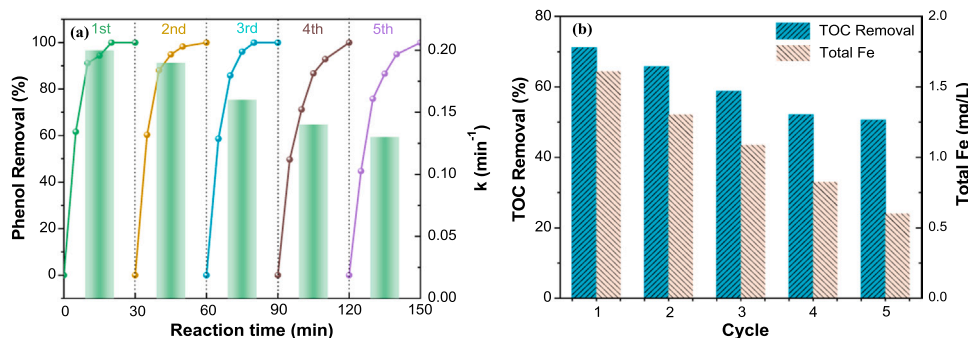


Fig. 11. (a) Phenol degradation and its k values; (b) TOC removal and Fe dissolution in various catalytic cycles. Conditions: $T = 293$ K; stirring speed = 400 rpm; initial pH = 5.8; [phenol] = 100 mg/L; [catalyst] = 0.2 g/L; $I = 50$ mA; in-gas O₃ concentration = 55 mg/L, gas flow = 25 mL min⁻¹.

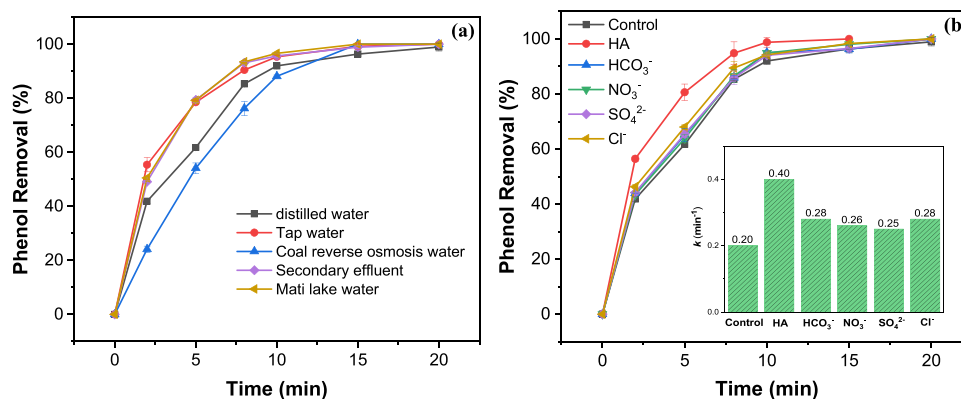


Fig. 12. Phenol degradation in (a) actual water; (b) 100 mg/L HA and inorganic ions. Conditions: $T = 293$ K; stirring speed = 400 rpm; initial pH = 5.8; [phenol] = 100 mg/L; [catalyst] = 0.2 g/L; $I = 50$ mA; in-gas O₃ concentration = 55 mg/L, gas flow = 25 mL min⁻¹.

100 mg/L humic acid (HA), the low (100 mg/L) and high concentration (10 g/L) anions such as bicarbonate (HCO₃⁻), chloride (Cl⁻), nitrate (NO₃⁻) and sulfate (SO₄²⁻) were separately added to the aqueous phenol solution. As shown in Fig. 12b, the addition of HA promoted the degradation of phenol evidently. The electrophilic addition of O₃ could be arisen to generate [•]OH because HA was consisted of the substances with electron-rich structures, which effectively accelerated the degradation of phenol with k from 0.20 min⁻¹ to 0.40 min⁻¹ in 20 min. And these anions displayed the slight promotion on the phenol removal in Fe⁰@CS/EP. [•]OH was converted into [•]CO₃ by HCO₃⁻ at rate constant of 8.5×10^6 M⁻¹s⁻¹ (HCO₃⁻ + [•]OH → [•]CO₃ + H₂O). The resulting [•]CO₃, with one-electron potential of 1.78 V (pH 7), could react with the electron-rich phenols with high second order rate constant of 10⁵ M⁻¹s⁻¹ due to its selectivity, leading to the enhanced removal efficiency and accelerated the removal of phenol with k value from 0.20 min⁻¹ to 0.28 min⁻¹ in 20 min at 100 mg/L HCO₃⁻ [53]. In addition, it has been stated that

HCO₃⁻ could enhance the stability of aqueous molecular ozone, resulting in the presence of more ozone molecules available to degrade the pollutants [61]. In case of NO₃⁻ and SO₄²⁻, phenol degradation increased and the rate constant k increased from 0.20 min⁻¹ to 0.26 min⁻¹ and 0.25 min⁻¹ at 100 mg/L, respectively. These promotion effects might be attributed to the generation of free radicals such as [•]NO₃ and [•]SO₄ (NO₃⁻/SO₄²⁻ + [•]OH → [•]NO₃/[•]SO₄ + OH⁻), which were also involved in the degradation of phenol [34,36]. And Cl⁻ in the solution could be oxidized rapidly to form Cl₂ at DSA anode, and then was transformed into the active chlorine radical, which exerted a more remarkable effect on phenol degradation. It was also enhanced with the k value increasing from 0.20 min⁻¹ to 0.28 min⁻¹ in the presence of 100 mg/L Cl⁻ [53]. When the concentration of these anions reached 10 g/L, the degradation of phenol was still improved (Fig. S16). In particular, Cl⁻ has the greatest promoting effect at 10 g/L with k of 0.33 min⁻¹.

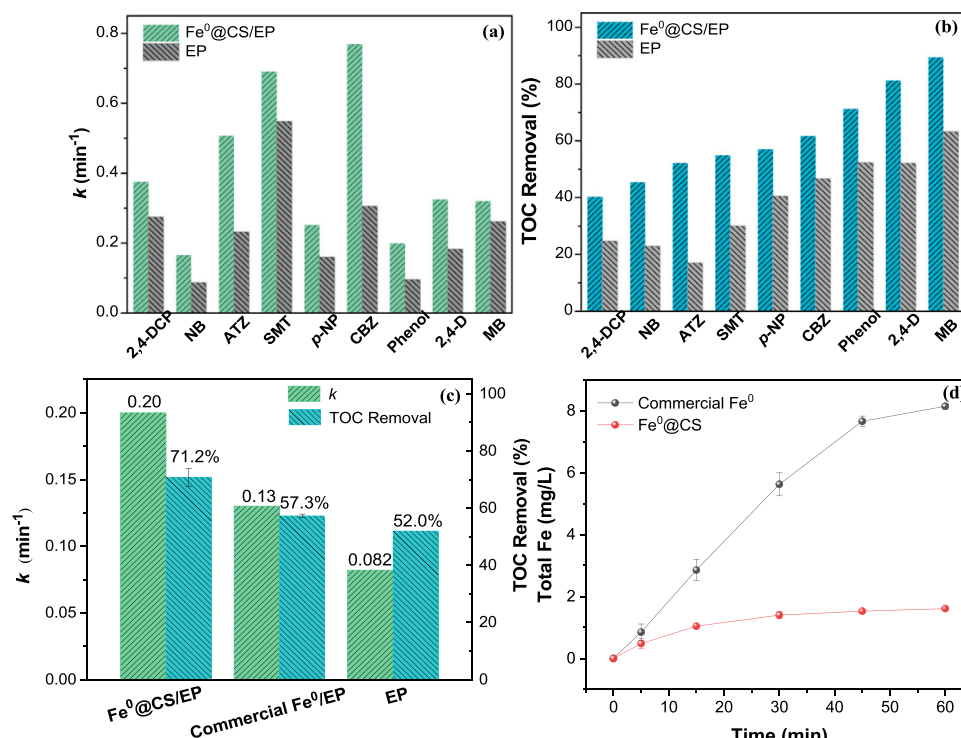


Fig. 13. (a) The degradation rate constant and (b) TOC removal of (a and b) different pollutants in EP and Fe⁰@CS/EP; (c) commercial Fe⁰ and Fe⁰@CS in EP and (d) the total Fe dissolution. Conditions: $T = 293$ K; stirring speed = 400 rpm; [catalyst] = 0.2 g/L; [ATZ] = 50 mg/L; other organic concentration = 100 mg/L; $I = 50$ mA; in-gas O₃ concentration = 55 mg/L, gas flow = 25 mL min⁻¹.

3.8.2. Applicability of various pollutants

The Fe⁰@CS/EP process was compared with EP for its ability to remove 2,4-DCP, NB, ATZ, SMT, *p*-NP, CBZ, phenol, 2,4-D, and MB from aqueous solution. By the Fe⁰@CS/EP process, 2,4-DCP, ATZ, SMT, CBZ, 2,4-D and MB could be completely removed within 15 min, while the removal of NB, *p*-NP and phenol and reached 88.92%, 97.01% and 94.41%, and their removals were near 100% at 30 min. But by the EP process, their removals were all inadequate after 15 min, i.e., NB (63.35%), ATZ (96.93%), *p*-NP (82.11%), phenol (75.21%), 2,4-D (86.11%) and MB (97.91%). Fig. S17 presented that the degradation followed pseudo-first-order kinetics. The *k* value of the Fe⁰@CS/EP process were 1.3–2 folds higher than those in EP, which were 0.38, 0.17, 0.51, 0.69, 0.25, 0.77, 0.20, 0.32 and 0.32 min⁻¹ for the removal of 2,4-DCP, NB, ATZ, SMT, *p*-NP, CBZ, phenol, 2,4-D, and MB respectively (Fig. 13a). As shown in Fig. 13b, a greater mineralization was also obtained in Fe⁰@CS/EP, in which the TOC removal of 2,4-DCP, NB, ATZ, SMT, *p*-NP, CBZ, phenol, 2, 4-D and MB were up to 40.26%, 45.42%, 52.2%, 54.92%, 57.06%, 61.73%, 71.23%, 81.25% and 89.41% at 60 min. But their mineralizations by EP process were 24.75%, 22.93%, 17.02%, 30.08%, 40.5%, 46.68%, 52.38%, 52.17%, and 63.25% at 60 min, respectively. The mineralization efficiency of phenolic pollutants (2,4-DCP, *p*-NP, phenol), pesticide (ATZ and 2, 4-D), PPCPs (SMT and CBZ), NB and MB increased by 0.62–0.36 folds, 2.07 and 0.42 folds, 0.83 and 0.32 folds, 0.98 and 0.41 folds, respectively. The comparison results displayed the wide effectiveness on water purification of Fe⁰@CS/EP process, which might be attributed to the promotion effect of catalytic reaction with O₃ and H₂O₂ by Fe⁰@CS [47].

3.8.3. Comparison with the commercial Fe⁰

This efficient performance of the Fe⁰@CS was also compared with the commercial Fe⁰ (micron-scale) in strengthened EP process. According to Table S2, Fe⁰@CS contained 4 wt% Fe. Therefore, 0.008 g/L commercial Fe⁰ was added into EP. As shown in Figs. 13c and 13d, the *k* of phenol degradation by EP and Fe⁰/EP process at 30 min and TOC removal at 60 min was only 0.082 min⁻¹ and 0.13 min⁻¹, 52.0% and 57.3%. However, the rate constant and TOC removal in Fe⁰@CS/EP increased to 0.20 min⁻¹ and 71.2%. In addition, the Fe dissolution of Fe⁰@CS was 1.6 mg/L, fifth part of the commercial Fe⁰ (8.1 mg/L) in 60 min. On the whole, Fe⁰@CS was environmentally effective heterogeneous catalyst for reinforcing EP process.

4. Conclusions

In this work, PR@Fe_xO_y was calcined at high temperatures in Ar atmosphere to synthesize the Fe⁰ embedded in porous carbon sphere, which could effectively activate O₃ and H₂O₂ to remove various organic pollutants in Fe⁰@CS/EP. The addition of Fe⁰@CS broadened pH application range of EP technology evidently. There were the active species such as •OH, •O₂, ¹O₂ in Fe⁰@CS/EP, in which •OH was dominant. Moreover, the contribution of various reactions (catalytic ozonation, Fenton-like, peroxone and direct molecule ozone oxidation) to phenol degradation was evaluated quantitatively. Fe⁰@CS could be oxidized by O₃ and H₂O₂ due to its porous structure, and H₂O₂ played a leading role in the corrosion of Fe⁰ embedded in carbon spheres. The generated ≡Fe²⁺ could effectively activate O₃ and H₂O₂ for raising the treatment efficiency of pollutants. Moreover, the protection of carbon spheres effectively reduced the Fe dissolution in strong oxidizing environment. Simultaneously, the porous spherical structure of Fe⁰@CS enhanced the mass transfer of reactants among O₃, H₂O₂ and pollutants. In this work, the possible degradation pathway and toxicity assessment of phenol by Fe⁰@CS/EP was also put forward. This study provided an ideology for the safe application of Fe⁰ in augmenting the EP process with reducing Fe dissolution.

Declaration of Competing Interest

The authors declare that they have no known competing financial interests or personal relationships that could have appeared to influence the work reported in this paper.

Data Availability

The data that has been used is confidential.

Acknowledgments

This work was financially supported by Natural Science Foundation of China (nos. 21976096 and 52170085), Tianjin Development Program for Innovation and Entrepreneurship, Key Project of Natural Science Foundation of Tianjin (no. 21JCZDJC00320), National Key Research and Development Program International Cooperation Project (2021YFE0106500), National High-level Foreign Experts Project (QN20200002003, G2021125001 and G2021125002), and Fundamental Research Funds for the Central Universities, Nankai University.

Appendix A. Supporting information

Supplementary data associated with this article can be found in the online version at doi:10.1016/j.apcatb.2022.121935.

References

- [1] L. Lyu, L. Zhang, Q. Wang, Y. Nie, C. Hu, Enhanced Fenton catalytic efficiency of gamma-Cu-Al₂O₃ by sigma-Cu²⁺-ligand complexes from aromatic pollutant degradation, *Environ. Sci. Technol.* 49 (2015) 8639–8647.
- [2] Y. Long, J. Dai, S. Zhao, Y. Su, Z. Wang, Z. Zhang, Atomically dispersed cobalt sites on graphene as efficient periodate activators for selective organic pollutant degradation, *Environ. Sci. Technol.* 55 (2021) 5357–5370.
- [3] S. Deng, L. Jothinathan, Q. Cai, R. Li, M. Wu, S.L. Ong, J. Hu, FeO_x@GAC catalyzed microbubble ozonation coupled with biological process for industrial phenolic wastewater treatment: Catalytic performance, biological process screening and microbial characteristics, *Water Res.* 190 (2021), 116687.
- [4] D. He, H. Niu, S. He, L. Mao, Y. Cai, Y. Liang, Strengthened Fenton degradation of phenol catalyzed by core/shell Fe-Pd@C nanocomposites derived from mechanochemically synthesized Fe-Metal organic frameworks, *Water Res.* 162 (2019) 151–160.
- [5] X. Wang, J. Jing, M. Zhou, R. Dewil, Recent advances in H₂O₂-based advanced oxidation processes for removal of antibiotics from wastewater, *Chin. Chem. Lett.* (2022).
- [6] T.M. Lesko, A.J. Colussi, M.R. Hoffmann, Hydrogen isotope effects and mechanism of aqueous ozone and peroxone decompositions, *J. Am. Chem. Soc.* 126 (2004) 4432–4436.
- [7] L. Dobelle, S. Kim, A.X. LeVan, H. Leandri, M.R. Hoffmann, C.A. Cid, Onsite graywater treatment in a two-stage electro-peroxone reactor with a partial recycle of treated effluent, *ACS EST Eng.* 1 (2021) 1659–1667.
- [8] X. Li, Y. Wang, S. Yuan, Z. Li, B. Wang, J. Huang, S. Deng, G. Yu, Degradation of the anti-inflammatory drug ibuprofen by electro-peroxone process, *Water Res.* 63 (2014) 81–93.
- [9] H. Wang, J. Zhan, W. Yao, B. Wang, S. Deng, J. Huang, G. Yu, Y. Wang, Comparison of pharmaceutical abatement in various water matrices by conventional ozonation, peroxone (O₃/H₂O₂), and an electro-peroxone process, *Water Res.* 130 (2018) 127–138.
- [10] W. Yao, Q. Qu, U. von Gunten, C. Chen, G. Yu, Y. Wang, Comparison of methylisoborneol and geosmin abatement in surface water by conventional ozonation and an electro-peroxone process, *Water Res.* 108 (2017) 373–382.
- [11] J. Yao, B. Yu, H. Li, Y. Yang, Interfacial catalytic and mass transfer mechanisms of an electro-peroxone process for selective removal of multiple fluoroquinolones, *Appl. Catal. B Environ.* 298 (2021), 120608.
- [12] S. Li, J. Huang, Z. Ye, Y. Wang, X. Li, J. Wang, L. Li, The mechanism of Metal-H₂O₂ complex immobilized on MCM-48 and enhanced electron transfer for effective peroxone ozonation of sulfamethazine, *Appl. Catal. B Environ.* 280 (2021), 119453.
- [13] D. Wu, G. Lu, J. Yao, C. Zhou, F. Liu, J. Liu, Adsorption and catalytic electro-peroxone degradation of fluconazole by magnetic copper ferrite/carbon nanotubes, *Chem. Eng. J.* 370 (2019) 409–419.
- [14] M. Kohantorabi, G. Moussavi, P. Oulego, S. Giannakis, Heterogeneous catalytic ozonation and peroxone-mediated removal of Acetaminophen using natural and modified hematite-rich soil, as efficient and environmentally friendly catalysts, *Appl. Catal. B Environ.* 301 (2022), 120786.
- [15] S. Li, J. Huang, Y. Wang, G. Yu, Role of in-situ electro-generated H₂O₂•••bridge in tetracycline degradation governed by mechanochemical Si-O anchoring Cu²⁺ as

- electron shuttle during E-peroxone process, *Appl. Catal. B Environ.* 304 (2022), 120930.
- [16] Z. Xiong, B. Lai, P. Yang, Insight into a highly efficient electrolysis-ozone process for N,N-dimethylacetamide degradation: quantitative analysis of the role of catalytic ozonation, fenton-like and peroxone reactions, *Water Res.* 140 (2018) 12–23.
 - [17] F. Wang, Y. Huang, P. Wen, Q. Li, Transformation mechanisms of refractory organic matter in mature landfill leachate treated using an Fe⁰-participated O₃/H₂O₂ process, *Chemosphere* 263 (2021), 128198.
 - [18] Y. Pan, Y. Zhang, M. Zhou, J. Cai, Y. Tian, Enhanced removal of antibiotics from secondary wastewater effluents by novel UV/pre-magnetized Fe⁰/H₂O₂ process, *Water Res.* 153 (2019) 144–159.
 - [19] Z. Xiong, B. Lai, Y. Yuan, J. Cao, P. Yang, Y. Zhou, Degradation of p-nitrophenol (p-NP) in aqueous solution by a micro-size Fe⁰/O₃ process (mFe⁰/O₃): optimization, kinetic, performance and mechanism, *Chem. Eng. J.* 302 (2016) 137–145.
 - [20] M. Kallel, C. Belaid, R. Boussahel, M. Ksibi, A. Montiel, B. Elleuch, Olive mill wastewater degradation by Fenton oxidation with zero-valent iron and hydrogen peroxide, *J. Hazard. Mater.* 163 (2009) 550–554.
 - [21] F. Wang, Y. Luo, G. Ran, Q. Li, Sequential coagulation and Fe⁰-O₃/H₂O₂ process for removing recalcitrant organics from semi-aerobic aged refuse biofilter leachate: Treatment efficiency and degradation mechanism, *Sci. Total Environ.* 699 (2020), 134371.
 - [22] H. Lv, H. Niu, X. Zhao, Y. Cai, F. Wu, Carbon zero-valent iron materials possessing high-content fine Fe⁰ nanoparticles with enhanced microelectrolysis-Fenton-like catalytic performance for water purification, *Appl. Catal. B: Environ.* 286 (2021), 119940.
 - [23] J. Li, H. Lan, H. Liu, G. Zhang, X. An, R. Liu, J. Qu, Intercalation of nanosized Fe₃C in iron/carbon to construct multifunctional interface with reduction, catalysis, corrosion resistance, and immobilization capabilities, *ACS Appl. Mater. Interfaces* 11 (2019) 15709–15717.
 - [24] Z. Jiang, L. Lv, W. Zhang, Q. Du, B. Pan, L. Yang, Q. Zhang, Nitrate reduction using nanosized zero-valent iron supported by polystyrene resins: Role of surface functional groups, *Water Res.* 45 (2011) 2191–2198.
 - [25] H. Zhang, O. Noonan, X. Huang, Y. Yang, C. Xu, L. Zhou, C. Yu, Surfactant-free assembly of mesoporous carbon hollow spheres with large tunable pore sizes, *ACS Nano* 10 (2016) 4579–4586.
 - [26] L. Xie, M. Yan, T. Liu, K. Gong, X. Luo, B. Qiu, J. Zeng, Q. Liang, S. Zhou, Y. He, W. Zhang, Y. Jiang, Y. Yu, J. Tang, K. Liang, D. Zhao, B. Kong, Kinetics-controlled super-assembly of asymmetric porous and hollow carbon nanoparticles as light-sensitive smart nanovehicles, *J. Am. Chem. Soc.* 144 (2022) 1634–1646.
 - [27] S. Chen, Z. Chen, S. Siahrostami, T.R. Kim, D. Nordlund, D. Sokaras, S. Nowak, J. W.F. To, D. Higgins, R. Sinclair, J.K. Nørskov, T.F. Jaramillo, Z. Bao, Defective carbon-based materials for the electrochemical synthesis of hydrogen peroxide, *ACS Sustain. Chem. Eng.* 6 (2017) 311–317.
 - [28] F. Li, L. Xie, G. Sun, Q. Kong, F. Su, Y. Cao, J. Wei, A. Ahmad, X. Guo, C.-M. Chen, Resorcinol-formaldehyde based carbon aerogel: preparation, structure and applications in energy storage devices, *Microporous Mesoporous Mater.* 279 (2019) 293–315.
 - [29] F. Xiao, Z. Wang, J. Fan, T. Majima, H. Zhao, G. Zhao, Selective electrocatalytic reduction of oxygen to hydroxyl radicals via 3-electron pathway with FeCo alloy encapsulated carbon aerogel for fast and complete removing pollutants, *Angew. Chem. Int. Ed.* 60 (2021) 10375–10383.
 - [30] Y. Pang, K. Wang, H. Xie, Y. Sun, M.-M. Titirici, G.-L. Chai, Mesoporous carbon hollow spheres as efficient electrocatalysts for oxygen reduction to hydrogen peroxide in neutral electrolytes, *ACS Catal.* 10 (2020) 7434–7442.
 - [31] H. Sun, G. Zhou, S. Liu, H.M. Ang, M.O. Tade, S. Wang, Nano-Fe⁰ encapsulated in microcarbon spheres: synthesis, characterization, and environmental applications, *ACS Appl. Mater. Interfaces* 4 (2012) 6235–6241.
 - [32] T. Wang, J. Zhang, Y. Song, Z. Liu, H. Ding, C. Zhao, P. Wang, Role of micro-size zero valence iron as particle electrodes in a three-dimensional heterogeneous electro-ozonation process for nitrobenzene degradation, *Chemosphere* 276 (2021), 130264.
 - [33] J. Xie, X. Li, W. Chen, X. Sun, K. Chen, Y. Tang, L. Li, Enhanced mineralization of oxalate by heterogeneous peroxone: the interfacial reaction on the core-shell CeO_x/SiO₂, *Chem. Eng. J.* 379 (2020), 122344.
 - [34] B. Kakavandi, S. Alavi, F. Ghanbari, M. Ahmadi, Bisphenol A degradation by peroxymonosulfate photo-activation coupled with carbon-based cobalt ferrite nanocomposite: performance, upgrading synergy and mechanistic pathway, *Chemosphere* 287 (2022), 132024.
 - [35] S. Moradi, A.A. Isari, F. Hayati, R. Rezaei Kalantary, B. Kakavandi, Co-implanting of TiO₂ and liquid-phase-delaminated g-C₃N₄ on multi-functional graphene nanobridges for enhancing photocatalytic degradation of acetaminophen, *Chem. Eng. J.* 414 (2021), 128618.
 - [36] M. Moradi, B. Kakavandi, A. Bahadoran, S. Giannakis, E. Dehghanifard, Intensification of persulfate-mediated elimination of bisphenol A by a spinel cobalt ferrite-anchored g-C₃N₄S-scheme photocatalyst: catalytic synergies and mechanistic interpretation, *Sep. Purif. Technol.* 285 (2022), 120313.
 - [37] Y. Song, C. Zhao, T. Wang, Z. Kong, L. Zheng, H. Ding, Y. Liu, H. Zheng, Simultaneously promoted reactive manganese species and hydroxyl radical generation by electro-permanganate with low additive ozone, *Water Res.* 189 (2021), 116623.
 - [38] J. Wang, X. Quan, S. Chen, H. Yu, G. Liu, Enhanced catalytic ozonation by highly dispersed CeO₂ on carbon nanotubes for mineralization of organic pollutants, *J. Hazard. Mater.* 368 (2019) 621–629.
 - [39] Q. Zhang, M. Zhou, Z. Lang, X. Du, J. Cai, L. Han, Dual strategies to enhance mineralization efficiency in innovative electrochemical advanced oxidation processes using natural air diffusion electrode: Improving both H₂O₂ production and utilization efficiency, *Chem. Eng. J.* 413 (2021), 127564.
 - [40] X. Du, Hm Yang, Yl Zhang, Qc Hu, Sb Li, Wx He, Synthesis of size-controlled carbon microspheres from resorcinol/formaldehyde for high electrochemical performance, *New Carbon Mater.* 36 (3) (2021) 616–624.
 - [41] D. Kim, N.P. Zussblatt, H.T. Chung, S.M. Becwar, P. Zelenay, B.F. Chmelka, Highly graphitic mesoporous Fe, N-doped carbon materials for oxygen reduction electrochemical catalysts, *ACS Appl. Mater. Interfaces* 10 (2018) 25337–25349.
 - [42] P. Su, X. Du, Y. Zheng, W. Fu, Q. Zhang, M. Zhou, Interface-confined multi-layered reaction centers between Ce-MOFs and Fe₃O₄@C for heterogeneous electro-Fenton at wide pH 3–9: mediation of Ce³⁺/Ce⁴⁺ and oxygen vacancy, *Chem. Eng. J.* 433 (2022), 133597.
 - [43] X. Du, W. Fu, P. Su, Q. Zhang, M. Zhou, S-doped MIL-53 as efficient heterogeneous electro-Fenton catalyst for degradation of sulfamethazine at circumneutral pH, *J. Hazard. Mater.* 424 (2022), 127674.
 - [44] X. Du, M. Zhou, Strategies to enhance catalytic performance of metal organic frameworks in sulfate radical-based advanced oxidation processes for organic pollutants removal, *Chem. Eng. J.* 403 (2021), 126346.
 - [45] C. Ouyang, K. Wei, X. Huang, M. Gamal El-Din, X. Zhang, Bifunctional Fe for induced graphitization and catalytic ozonation based on a Fe/N-doped carbon Al₂O₃ framework: theoretical calculations guided catalyst design and optimization, *Environ. Sci. Technol.* 55 (2021) 11236–11244.
 - [46] Y. Tian, W. Fu, Q. Wang, Y. Tang, M. Zhou, High electron transfer rate and efficiency on Fe⁰ modified by sulfidation and pre-magnetization for carbamazepine degradation by heterogeneous electro-Fenton in wide pH ranges, *Chem. Eng. J.* 427 (2022), 131694.
 - [47] W. Chen, J. Xie, X. Li, L. Li, Oxygen vacancies and Lewis sites activating O₃/H₂O₂ at wide pH range via surface electron transfer over CeO_x@SiO₂ for nitrobenzene mineralization, *J. Hazard. Mater.* 406 (2021), 124766.
 - [48] G. Xia, H. Wang, J. Zhan, X. Yin, X. Wu, G. Yu, Y. Wang, M. Wu, Evaluation of the stability of polyacrylonitrile-based carbon fiber electrode for hydrogen peroxide production and phenol mineralization during electro-peroxone process, *Chem. Eng. J.* 396 (2020), 125291.
 - [49] A. Shokri, Employing electro-peroxone process for degradation of Acid Red 88 in aqueous environment by Central Composite Design: A new kinetic study and energy consumption, *Chemosphere* 296 (2022), 133817.
 - [50] S. Li, J. Huang, Y. Wang, G. Yu, Role of in-situ electro-generated H₂O₂—bridge in tetracycline degradation governed by mechanochemical Si-O anchoring Cu²⁺ as electron shuttle during E-peroxone process, *Appl. Catal. B: Environ.* 304 (2022), 120930.
 - [51] W. Xie, Z. Huang, F. Zhou, Y. Li, X. Bi, Q. Bian, S. Sun, Heterogeneous Fenton-like degradation of amoxicillin using MOF-derived Fe⁰ embedded in mesoporous carbon as an effective catalyst, *J. Clean. Prod.* 313 (2021), 127754.
 - [52] W. Yao, J. Fu, H. Yang, G. Yu, Y. Wang, The beneficial effect of cathodic hydrogen peroxide generation on mitigating chlorinated by-product formation during water treatment by an electro-peroxone process, *Water Res.* 157 (2019) 209–217.
 - [53] A. Asghar, H.V. Lutze, J. Tuerk, T.C. Schmidt, Influence of water matrix on the degradation of organic micropollutants by ozone based processes: a review on oxidant scavenging mechanism, *J. Hazard. Mater.* 429 (2022), 128189.
 - [54] Y. Wang, X. Duan, Y. Xie, H. Sun, S. Wang, Nanocarbon-based catalytic ozonation for aqueous oxidation: engineering defects for active sites and tunable reaction pathways, *ACS Catal.* 10 (2020) 13383–13414.
 - [55] L. Zhou, S. Zhang, Z. Li, X. Liang, Z. Zhang, R. Liu, J. Yun, Efficient degradation of phenol in aqueous solution by catalytic ozonation over MgO/AC, *J. Water Process Eng.* 36 (2020), 101168.
 - [56] Y. Pan, R. Qin, M. Hou, J. Xue, M. Zhou, L. Xu, Y. Zhang, The interactions of polyphenols with Fe and their application in Fenton/Fenton-like reactions, *Sep. Purif. Technol.* 300 (2022), 121831.
 - [57] Z. Wu, M. Zhou, Partial degradation of phenol by advanced electrochemical oxidation process, *Environ. Sci. Technol.* 35 (2001) 2698–2703.
 - [58] M.S.S. Abujazar, S.U. Karaa, S.S. Abu Amr, M.Y.D. Alazaiza, M.J.K. Bashir, Recent advancement in the application of hybrid coagulants in coagulation-flocculation of wastewater: A review, *J. Clean. Prod.* 345 (2022), 131133.
 - [59] An Demarca, B. Erdozan, R. Azcamder, Wastewater treatment at the petroleum refinery, Kırıkkale, Turkey using some coagulants and Turkish clays as coagulant aids, *Water Res.* 32 (1998) 3495–3499.
 - [60] Q.Y. Wu, Z.W. Yang, Y. Du, W.Y. Ouyang, W.L. Wang, The promotions on radical formation and micropollutant degradation by the synergies between ozone and chemical reagents (synergistic ozonation): a review, *J. Hazard. Mater.* 418 (2021), 126327.
 - [61] J.E. Grebel, J.J. Pignatello, W.A. Mitch, Effect of halide ions and carbonates on organic contaminant degradation by hydroxyl radical-based advanced oxidation processes in saline waters, *Environ. Sci. Technol.* 44 (2010) 6822–6828.